



TOI-503: The First Known Brown-dwarf Am-star Binary from the *TESS* Mission*

Ján Šubjak^{1,2}, Rishikesh Sharma³, Theron W. Carmichael^{4,5,51}, Marshall C. Johnson⁶, Erica J. Gonzales^{7,51}, Elisabeth Matthews⁸, Henri M. J. Boffin⁹, Rafael Brahm^{10,11,12}, Priyanka Chaturvedi¹³, Abhijit Chakraborty³, David R. Ciardi¹⁴, Karen A. Collins⁵, Massimiliano Esposito¹³, Malcolm Fridlund^{15,16}, Tianjun Gan¹⁷, Davide Gandolfi¹⁸, Rafael A. García^{19,20}, Eike Guenther¹³, Artie Hatzes¹³, David W. Latham⁵, Stéphane Mathis^{19,20}, Savita Mathur^{21,22}, Carina M. Persson¹⁵, Howard M. Relles⁵, Joshua E. Schlieder²³, Thomas Barclay²⁴, Courtney D. Dressing²⁵, Ian Crossfield⁸, Andrew W. Howard²⁶, Florian Rodler²⁷, George Zhou⁵, Samuel N. Quinn⁵, Gilbert A. Esquerdo⁵, Michael L. Calkins⁵, Perry Berlind⁵, Keivan G. Stassun^{28,29}, Martin Blažek^{1,30}, Marek Skarka^{1,30}, Magdalena Špoková^{1,30}, Jiří Žák³⁰, Simon Albrecht³¹, Roi Alonso Sobrino^{21,22}, Paul Beck^{21,22,32}, Juan Cabrera³³, Ilaria Carleo³⁴, William D. Cochran³⁵, Szilard Csizmadia³³, Fei Dai^{8,36}, Hans J. Deeg^{21,22}, Jerome P. de Leon³⁷, Philipp Eigmüller³³, Michael Endl³⁵, Anders Erikson³³, Akihiko Fukui^{38,39,40}, Iskra Georgieva¹⁵, Lucía González-Cuesta^{21,22}, Sascha Grziwa⁴¹, Diego Hidalgo^{21,22}, Teruyuki Hirano⁴², Maria Hjorth³², Emil Knudstrup³², Judith Korth⁴¹, Kristine W. F. Lam⁴³, John H. Livingston³⁷, Mikkel N. Lund³¹, Rafael Luque^{21,22}, Pilar Montanes Rodríguez^{21,22}, Felipe Murgas^{21,22}, Norio Narita^{21,38,44,45}, David Nespral^{21,22}, Prajwal Niraula⁴⁶, Grzegorz Nowak^{21,22}, Enric Pallé^{21,22}, Martin Pätzold⁴¹, Jorge Prieto-Arranz^{21,22}, Heike Rauer^{33,47,48}, Seth Redfield³⁴, Ignasi Ribas^{49,50}, Alexis M. S. Smith³³, Vincent Van Eylen³⁶, and Petr Kabáth¹

¹ Astronomical Institute, Czech Academy of Sciences, Fričova 298, 251 65, Ondřejov, Czech Republic

² Astronomical Institute of Charles University, V Holešovičkách 2, 180 00, Praha, Czech Republic

³ Astronomy & Astrophysics Division, Physical Research Laboratory, Ahmedabad 380009, India

⁴ Harvard University, Cambridge, MA 02138, USA

⁵ Center for Astrophysics|Harvard & Smithsonian, 60 Garden Street, Cambridge, MA 02138, USA

⁶ Las Cumbres Observatory, 6740 Cortona Drive, Suite 102, Goleta, CA 93117, USA

⁷ University of California, Santa Cruz, 1156 High Street, Santa Cruz CA 95065, USA

⁸ Department of Physics, and Kavli Institute for Astrophysics and Space Research, Massachusetts Institute of Technology, Cambridge, MA 02139, USA

⁹ ESO, Karl-Schwarzschild-Straße 2, D-85748 Garching bei München, Germany

¹⁰ Center of Astro-Engineering UC, Pontificia Universidad Católica de Chile, Av. Vicuña Mackenna 4860, 7820436 Macul, Santiago, Chile

¹¹ Instituto de Astrofísica, Pontificia Universidad Católica de Chile, Av. Vicuña Mackenna 4860, Macul, Santiago, Chile

¹² Millennium Institute for Astrophysics, Chile

¹³ Thüringer Landessternwarte Tautenburg, Sternwarte 5, D-07778 Tautenburg, Germany

¹⁴ Caltech/IPAC-NASA Exoplanet Science Institute, M/S 100-22, 770 S. Wilson Avenue, Pasadena, CA 91106, USA

¹⁵ Chalmers University of Technology, Department of Space, Earth and Environment, Onsala Space Observatory, SE-439 92 Onsala, Sweden

¹⁶ Leiden Observatory, University of Leiden, P.O. Box 9513, 2300 RA, Leiden, The Netherlands

¹⁷ Physics Department and Tsinghua Centre for Astrophysics, Tsinghua University, Beijing 100084, People's Republic of China

¹⁸ Dipartimento di Fisica, Università degli Studi di Torino, via Pietro Giuria 1, I-10125, Torino, Italy

¹⁹ IRFU, CEA, Université Paris-Saclay, Gif-sur-Yvette, France

²⁰ AIM, CEA, CNRS, Université Paris-Saclay, Université Paris Diderot, Sorbonne Paris Cité, F-91191 Gif-sur-Yvette, France

²¹ Instituto de Astrofísica de Canarias, C/ Vía Láctea s/n, E-38205 La Laguna, Spain

²² Departamento de Astrofísica, Universidad de La Laguna, E-38206 La Laguna, Spain

²³ Exoplanets and Stellar Astrophysics Laboratory, Code 667, NASA Goddard Space Flight Center, Greenbelt, MD 20771, USA

²⁴ NASA Goddard Space Flight Center, Greenbelt, MD 20771, USA

²⁵ Astronomy Department, University of California, Berkeley, CA 94720, USA

²⁶ California Institute of Technology, Pasadena, CA 91125, USA

²⁷ European Southern Observatory, Alonso de Córdova 3107, Vitacura, Santiago, Chile

²⁸ Vanderbilt University, Department of Physics & Astronomy, 6301 Stevenson Center Lane, Nashville, TN 37235, USA

²⁹ Fisk University, Department of Physics, 1000 18th Avenue North, Nashville, TN 37208, USA

³⁰ Department of Theoretical Physics and Astrophysics, Masaryk University, Kotlářská 2, 61137 Brno, Czech Republic

³¹ Stellar Astrophysics Centre, Department of Physics and Astronomy, Aarhus University, Ny Munkegade 120, DK-8000 Aarhus C, Denmark

³² Institut für Physik, Karl-Franzens University of Graz, Universitätsplatz 5, A-8020 Graz, Austria

³³ Institute of Planetary Research, German Aerospace Center, Rutherfordstrasse 2, D-12489 Berlin, Germany

³⁴ Astronomy Department and Van Vleck Observatory, Wesleyan University, Middletown, CT 06459, USA

³⁵ Department of Astronomy and McDonald Observatory, University of Texas at Austin, 2515 Speedway, Stop C1400, Austin, TX 78712, USA

³⁶ Department of Astrophysical Sciences, Princeton University, 4 Ivy Lane, Princeton, NJ 08544, USA

³⁷ Department of Astronomy, The University of Tokyo, 7-3-1 Hongo, Bunkyo-ku, Tokyo 113-0033, Japan

³⁸ National Astronomical Observatory of Japan, 2-21-1 Osawa, Mitaka, Tokyo 181-8588, Japan

³⁹ Department of Earth and Planetary Science, Graduate School of Science, The University of Tokyo, 7-3-1 Hongo, Bunkyo-ku, Tokyo 113-0033, Japan

⁴⁰ Instituto de Astrofísica de Canarias, Vía Láctea s/n, E-38205 La Laguna, Tenerife, Spain

⁴¹ Rheinisches Institut für Umweltforschung an der Universität zu Köln, Aachener Strasse 209, D-50931 Köln, Germany

⁴² Department of Earth and Planetary Sciences, Tokyo Institute of Technology, 2-12-1 Ookayama, Meguro-ku, Tokyo 152-8551, Japan

⁴³ Zentrum für Astronomie und Astrophysik, Technische Universität Berlin, Hardenbergstr. 36, D-10623 Berlin, Germany

⁴⁴ Astrobiology Center, 2-21-1 Osawa, Mitaka, Tokyo 181-8588, Japan

⁴⁵ JST, PRESTO, 2-21-1 Osawa, Mitaka, Tokyo 181-8588, Japan

⁴⁶ Department of Earth, Atmospheric and Planetary Sciences, MIT, 77 Massachusetts Avenue, Cambridge, MA 02139, USA

⁴⁷ Center for Astronomy and Astrophysics, TU Berlin, Hardenbergstr. 36, D-10623 Berlin, Germany

⁴⁸ Institute of Geological Sciences, Freie Universität Berlin, Malteserstr. 74-100, D-12249 Berlin, Germany

* This work is done under the framework of the KESPRINT collaboration (<http://kesprint.science>). KESPRINT is an international consortium devoted to the characterization and research of exoplanets discovered with space-based missions.

⁴⁹ Institute of Space Sciences (ICE, CSIC), Campus UAB, C/Can Magrans, s/n, E-08193 Bellaterra, Spain⁵⁰ Institut d'Estudis Espacials de Catalunya (IEEC), Barcelona, Spain

Received 2019 September 16; revised 2019 December 23; accepted 2020 January 31; published 2020 March 27

Abstract

We report the discovery of an intermediate-mass transiting brown dwarf (BD), TOI-503b, from the *TESS* mission. TOI-503b is the first BD discovered by *TESS*, and it has circular orbit around a metallic-line A-type star with a period of $P = 3.6772 \pm 0.0001$ days. The light curve from *TESS* indicates that TOI-503b transits its host star in a grazing manner, which limits the precision with which we measure the BD's radius ($R_b = 1.34^{+0.26}_{-0.15} R_J$). We obtained high-resolution spectroscopic observations with the FIES, Ondřejov, PARAS, Tautenburg, and TRES spectrographs, and measured the mass of TOI-503b to be $M_b = 53.7 \pm 1.2 M_J$. The host star has a mass of $M_* = 1.80 \pm 0.06 M_\odot$, a radius of $R_* = 1.70 \pm 0.05 R_\odot$, an effective temperature of $T_{\text{eff}} = 7650 \pm 160$ K, and a relatively high metallicity of 0.61 ± 0.07 dex. We used stellar isochrones to derive the age of the system to be ~ 180 Myr, which places its age between that of RIK 72b (a ~ 10 Myr old BD in the Upper Scorpius stellar association) and AD 3116b (a ~ 600 Myr old BD in the Praesepe cluster). Given the difficulty in measuring the tidal interactions between BDs and their host stars, we cannot precisely say whether this BD formed in situ or has had its orbit circularized by its host star over the relatively short age of the system. Instead, we offer an examination of plausible values for the tidal quality factor for the star and BD. TOI-503b joins a growing number of known short-period, intermediate-mass BDs orbiting main-sequence stars, and is the second such BD known to transit an A star, after HATS-70b. With the growth in the population in this regime, the driest region in the BD desert ($35\text{--}55 M_J \sin i$) is reforesting.

Unified Astronomy Thesaurus concepts: Brown dwarfs (185); Stellar ages (1581); Am stars (33); Spectroscopy (1558); Transit photometry (1709); Radial velocity (1332); Stellar rotation (1629); Stellar astronomy (1583)

1. Introduction

Brown dwarfs (BDs) are loosely defined as the objects that separate giant planets from low-mass stars. This definition is based on the mass of BDs, which ranges from 11 to $16 M_J$ (the approximate mass at which deuterium fusion can be sustained) to $75\text{--}80 M_J$ (the approximate mass to sustain hydrogen fusion), and yet some of the most recent BD discoveries seem to blur these boundaries (Díaz et al. 2014; Zhou et al. 2019). The uncertainties in boundaries are caused by dependence on exact chemical composition of objects near these mass ranges (Baraffe et al. 2002; Spiegel et al. 2011). One particular feature of the BD population is the apparent low occurrence rate of BDs in close orbits (i.e., within 3 au) to stars in comparison to giant planets and stars. The apparent lack of short-period BDs is the so-called *BD desert* (e.g., Grether & Lineweaver 2006; Sahlmann et al. 2011). Although the population of BDs in this region has slowly grown in recent years (Csizmadia & CoRoT Team 2016), the gap remains significant. As every desert has a driest part, the existence of a driest part of the BD desert has been argued to be the mass range between $35 \leq M_J \sin i \leq 55$ for orbital periods under 100 days (Ma & Ge 2014). Some authors use the existence of this gap to motivate the idea that there are two separate BD populations that result from two different BD formation processes. In this case, the two processes are formation via core accretion in a protoplanetary disk (the way giant planets are thought to form) and formation by gravitational instability, which is how stars are thought to typically form.

For core accretion to take place, an object must form in specific conditions with a sufficient gas mass budget in order for a protoplanetary core to grow sufficiently massive enough to become a giant planet or BD. This growth can be efficient at scales greater than 0.5 au, and depending on initial conditions, the giant planet or BD may then migrate inward (Coleman et al. 2017). If significant migration occurs, then the object did not form in situ (very near to or at its current orbit). On the other

hand, if an object is on the order of $40 M_J$ or more, then core accretion would not have been efficient enough to grow a protoplanetary core to that mass (Mordasini et al. 2012). In this case, the massive object may have formed through disk fragmentation or instabilities as low-mass stars form, making in situ formation at a close-in orbit to the host star a more viable option than core accretion.

Regarding the current transiting BD population, we see this aforementioned gap centered at a mass of $42.5 M_J$ (Ma & Ge 2014). Different studies suggest suppressing the distinction between BDs and the coolest M stars given their similarities (Whitworth 2018), while others suggest that BDs and giant planets form a continuum based on their mass–density relation (Hatzes & Rauer 2015; Persson et al. 2019), which, in turn, implies that the range of giant planets spans $0.3\text{--}60 M_J$ or $0.3\text{--}73 M_J$, respectively. Given this variety of interpretations of what separates giant planets, BDs, and low-mass stars, each new, well-characterized BD system, especially the ones that reside in the driest part of the BD desert, will be important to understanding this population as a whole.

We search for transiting BDs in particular because of the extra information that is obtained from a transiting object. In many cases, given the reliability of our stellar models, we may precisely (i.e., on the order of a few percent) measure the radius and mass of a transiting or eclipsing companion. These two properties are fundamental to an object's physical behavior and evolution. This value is enhanced for transiting BDs, given that they are so uncommon and that the substellar evolutionary models that aspire to describe these objects stand to be more rigorously tested with a larger sample that has well-characterized masses and radii. With only a minimum mass provided by a radial velocity (RV) orbit, we cannot verify if a companion is truly a BD or something more massive, like a star. With only a radius that is derived from stellar models and a light curve, we cannot determine if the stellar companion is a giant planet, a BD, a low-mass star, some form of stellar activity, or a false positive. Only with RVs and photometry combined may we

⁵¹ National Science Foundation Graduate Research Fellow.

identify BDs and test the mass–radius predictions of substellar evolutionary models.

This is where space-based photometric survey missions are particularly useful and often one of the best options for characterization of short-period transiting BDs. This was the case for the *CoRoT* mission (Rouan et al. 1998) and the *Kepler/K2* missions (Borucki et al. 2010), which made enormous contribution to exoplanetary science. So far, we are seeing a similar impact from the *Transiting Exoplanet Survey Satellite* (*TESS*⁵²) mission (Ricker et al. 2015), and we expect this impact to grow not only in the realm of small exoplanets, but for the transiting BD population as well. One aspect of *TESS* that distinguishes it from *CoRoT* and *Kepler/K2* is the number of bright stars it will observe. This makes potential BD host stars more accessible to spectroscopic facilities that may be used in coordination with *TESS* as well as the *Gaia* mission (for precise parallaxes) to detect and characterize BDs. The endeavor to discover more BDs is aided further by the relatively deep transit depths of BDs around typical main-sequence stars and the relatively large semi-amplitude signals relevant to RV follow-up. In total, there are more than 2000 known BDs (e.g., Skrzypek et al. 2016), with approximately 400 of these in bound systems. Of these, only 21 transit their host stars (with an additional 2 in a BD binary, Stassun et al. 2006), which makes a nearly all-sky transit survey mission like *TESS* an important tool in expanding and exploring the transiting BD population.

In this paper, we report the discovery of TOI-503b, the first BD known to orbit a metallic-lined A star (Am star). We find that the age of 180 Myr for TOI-503 and the circular orbit of TOI-503b are only consistent with the circularization timescale of the system for certain values of the tidal quality factor for the star and BD. However, we cannot conclusively determine which of these values best describe the system, given the general uncertainty of the tidal evolution models used. This work is the result of a collaboration between the KESPRINT consortium (e.g., Gandolfi et al. 2019; Hjorth et al. 2019; Korth et al. 2019; Livingston et al. 2019; Palle et al. 2019; Persson et al. 2019), PARAS-PRL India (Chakraborty et al. 2014), and the Harvard–Smithsonian Center for Astrophysics. We describe the observations in Section 2, analyze the data in Section 3, and provide a final discussion in Section 4.

2. Observations

2.1. *TESS* Light Curves

TESS monitored TOI-503 at a 2-minute cadence from 2019 January 8 to February 1 (~24.5 days). There is a gap of 1.7 days during this time due to the transfer of data from the spacecraft. The *TESS* Input Catalog (TIC) ID of the source is 186812530 (Stassun et al. 2018b), and it was observed in CCD 3 of camera 1 in Sector 7. TOI-503 will not be observed in any upcoming sectors of the primary *TESS* mission. We use the publicly available Pre-search Data Conditioning Simple Aperture Photometry (PDCSAP; Stumpe et al. 2014; Smith et al. 2012) light curves at Mikulski Archive for Space Telescopes (MAST)⁵³ that are provided by the *TESS* Science Processing Operations Center (SPOC). The PDCSAP light curves have the systematics of the spacecraft removed. The

SPOC pipeline (Jenkins et al. 2016) was used to extract the light curve and associated uncertainties from the original scientific data. We normalize this light curve by dividing it by the median-smoothed flux, which can be seen in Figure 1. A total of 6 transits spaced at a period of ~3.7 days are visible with depths of ~4500 ppm. The *TESS* data validation reports (Jenkins et al. 2016) identify TOI-503 as the host of a planet candidate with an estimated radius of $1.13 \pm 0.28 R_J$ by fitting the *TESS* light curve and using host-star parameters from Stassun et al. (2018b). The basic parameters of the star are listed in Table 1.

2.2. Ground-based Light Curves

As part of the *TESS* Follow-up Observation Program (TFOP), additional ground-based photometry was carried out by the Sinistro camera on the Las Cumbres Observatory (LCO), Siding Spring Observatory (SSO) 1.0 m on 2019 March 19, the Santa Barbara Instrument Group (SBIG) camera on the LCO 0.4 m on 2019 March 19, the Chilean Hungarian Automated Telescope (CHAT) 0.7 m on 2019 March 22, and the *KeplerCam* instrument on the Fred Lawrence Whipple Observatory (FLWO) 1.2 m on 2019 April 25. The LCO-SSO observations were taken in the *Y*-band and confirmed that there are no nearby or background eclipsing binaries within 2'5 that were blended in the aperture of camera 1 from *TESS*. The transit was not detected by LCO-SSO due to the insufficient amount of out-of-transit baseline flux. The observations with SBIG show a clear ingress but do not extend long enough to show the egress of the transit due to the target star reaching a high airmass. A full on-time transit was detected by CHAT in the *iband* as well as the *KeplerCam* instrument in the *z* band. By independently fitting just the *KeplerCam* light curve using *AstroImageJ* (Collins et al. 2017), we find that the modeled transit center time is consistent with the time predicted by the public *TESS* ephemeris within 1σ uncertainty. We decide against incorporating any ground-based follow-up in our joint analysis due to the shallow nature of this transit and the low transit depth signal-to-noise ratio.

2.3. Contamination from Nearby Sources

The TFOP was also responsible for observations of TOI-503 with Gemini/NIRI on 2019 March 22, and again with Keck/NIRC2 (Wizinowich et al. 2000) on 2019 April 7 (Figure 2). In each case, observations were taken in NGS mode in the *Br-γ* filter with the target as the guide star. Images were dithered, such that a sky background could be constructed, with a square dithering pattern for the NIRI data and a 3-point pattern for the NIRC2 data to avoid the known noisy fourth quadrant. For each instrument we used the same basic reduction procedure: images were flat-fielded and sky-subtracted, and the dithered frames were aligned and co-added.

Sensitivity was determined by injecting simulated sources azimuthally around the primary target, at separations of integer multiples of the central source's full width at half maximum (Furlan et al. 2017). The brightness of each injected source was scaled until standard aperture photometry detected it with 5σ significance. The resulting brightness of the injected sources relative to the target set the contrast limits at that injection location. The final 5σ limit at each separation was determined from the average of all of the determined limits at that separation and the uncertainty on the limit was set by the rms dispersion of the azimuthal slices at a given radial distance. No

⁵² <https://heasarc.gsfc.nasa.gov/docs/teess/>

⁵³ <https://mast.stsci.edu/portal/Mashup/Clients/Mast/Portal.html>

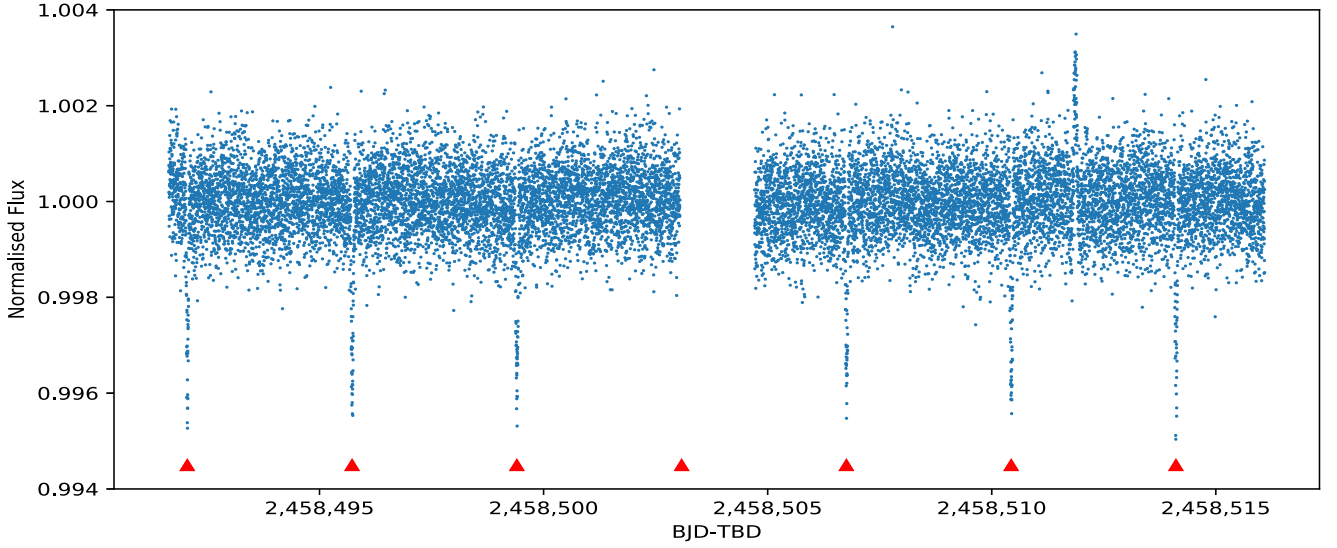


Figure 1. The normalized light curve of TOI-503 observed by *TESS* is plotted in blue, with red triangles denoting the time of each transit. Six transits can be seen spaced every ~ 3.7 days, with a depth of ~ 4500 ppm. The bump in the light curve around BJD 2458511.86 is a symmetric feature from the background, with a duration of roughly 3.5 hr. When excluding the star in an aperture, the bump is still visible, confirming its origin is not TOI-503.

Table 1
Basic Parameters for TOI-503

Parameter	Description	Value	Source
α_{J2000}	R.A.	08 17 16.89	(1)
δ_{J2000}	decl.	12 36 04.76	(1)
T	<i>TESS</i> T mag	9.187 ± 0.018	(2)
G	Gaia G mag	9.350 ± 0.002	(1)
B_T	Tycho B_T mag	9.703 ± 0.026	(3)
V_T	Tycho V_T mag	9.428 ± 0.024	(3)
J	2MASS J mag	8.945 ± 0.023	(4)
H	2MASS H mag	8.935 ± 0.017	(4)
K_S	2MASS K_S mag	8.895 ± 0.016	(4)
WISE1	WISE1 mag	8.868 ± 0.023	(5)
WISE2	WISE2 mag	8.885 ± 0.020	(5)
WISE3	WISE3 mag	8.888 ± 0.029	(5)
WISE4	WISE4 mag	8.558 ± 0.020	(5)
μ_δ	PM in R.A. (mas yr $^{-1}$)	-9.336 ± 0.095	(1)
μ_δ	PM in Decl. (mas yr $^{-1}$)	-9.945 ± 0.053	(1)
π	Parallax (mas)	3.887 ± 0.059	(1)
RV	Systemic RV (km s $^{-1}$)	29.469 ± 0.013	6

Other identifiers:

TIC 186812530
TYC 802-751-1
2MASS J08171689-1236049
Gaia DR2 650254479499119232

References. (1) Lindegren et al. (2018), (2) Stassun et al. (2018b), (3) Høg et al. (2000), (4) Cutri et al. (2003), (5) Cutri et al. (2013), (6) this work.

nearby contaminating sources are identified in either image, and at $1''$ we reach contrasts of $\Delta\text{mag} = 8.0$ mag in the NIRI data and $\Delta\text{mag} = 7.2$ mag in the NIRC2 data.

2.4. KESPRINT Spectra

We obtained a total of 50 spectra of TOI-503 between 2019 March 18, and 2019 April 17 using KESPRINT observing time on the 2 m Perek telescope at the Ondřejov Observatory, the 2 m Alfred Jensch telescope at Tautenburg, and the 2.56 m Nordic Optical Telescope (NOT) at the Roque de Los

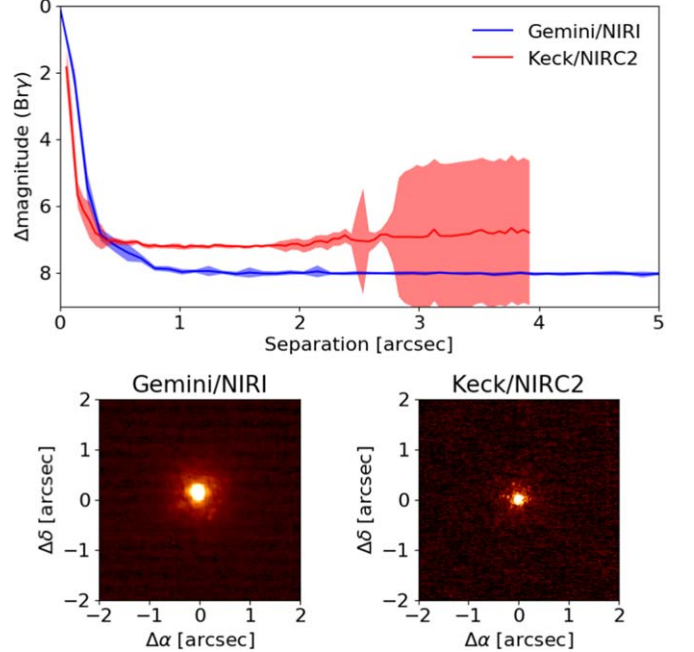


Figure 2. Sensitivity curve as a function of angular separation for TOI-503 from Gemini/NIRI and Keck/NIRC2. The inset shows the image of the target star from each instrument.

Muchachos Observatory. Using the central Europe monitoring network with telescopes in Ondřejov and Tautenburg for simultaneous observations has the advantage of allowing a better coverage of observing data. Furthermore, both telescopes are capable of long-term monitoring of interesting objects (Kabáth et al. 2019b). For these reasons, such observations are often performed (Kabáth et al. 2019a; Sabotta et al. 2019; Skarka et al. 2019). RVs from all used telescopes beyond the KESPRINT are reported in Table 2.

2.5. Ondřejov Spectra

We collected a set of 14 spectra using the Ondřejov Echelle Spectrograph, which has a spectral resolving power

Table 2

Multi-order Relative Radial Velocities of TOI-503 from Ondřejov, FIES, Tautenburg, TRES, and PARAS

BJD _{TDB} –2450,000	RV (m s ^{−1})	σ_{RV} (m s ^{−1})	Instrument
8566.651866	−24.9	84.6	TRES
8568.628445	8720.4	87.6	TRES
8569.654306	1721.4	76.6	TRES
8570.631553	1140.6	35.6	TRES
8571.619256	8129.6	52.7	TRES
8572.647920	6927.5	71.7	TRES
8573.712391	30.2	54.1	TRES
8574.660766	3615.3	65.4	TRES
8575.644821	9286.9	51.2	TRES
8576.674889	4227.1	59.9	TRES
8577.649209	−64.4	47.5	TRES
8587.709792	4140.1	63.7	TRES
8581.233706	−4877.9	92.1	PARAS
8582.207307	539.1	70.9	PARAS
8582.238727	805.1	88.6	PARAS
8583.212860	4393.9	85.7	PARAS
8583.242544	4175.4	100.8	PARAS
8584.201377	−1800.3	86.5	PARAS
8585.220041	−3730.9	87.4	PARAS
8564.408181	7370.8	250.5	ONDŘEJOV
8564.450341	7663.6	191.3	ONDŘEJOV
8565.411871	5208.5	292.7	ONDŘEJOV
8565.454031	4899.8	452.4	ONDŘEJOV
8566.414342	−1016.0	405.8	ONDŘEJOV
8572.314192	7360.1	391.9	ONDŘEJOV
8575.276802	6639.4	291.2	ONDŘEJOV
8575.369402	7511.8	227.1	ONDŘEJOV
8575.419602	7484.1	305.0	ONDŘEJOV
8578.300872	2048.7	274.6	ONDŘEJOV
8578.343032	2911.4	199.8	ONDŘEJOV
8578.385192	3016.4	222.3	ONDŘEJOV
8581.353282	−674.9	427.5	ONDŘEJOV
8581.395442	−829.4	409.7	ONDŘEJOV
8559.414221	−7002.3	212.0	TAUTENBURG
8561.366911	1000.0	80.0	TAUTENBURG
8562.458981	−6541.5	200.3	TAUTENBURG
8563.348001	−5693.6	143.8	TAUTENBURG
8567.360682	−3341.8	128.5	TAUTENBURG
8589.311442	−4202.8	160.8	TAUTENBURG
8589.326082	−3905.7	160.8	TAUTENBURG
8589.340732	−4058.3	82.7	TAUTENBURG
8590.312772	1848.7	200.9	TAUTENBURG
8590.326992	1853.5	185.5	TAUTENBURG
8590.341222	1665.8	273.4	TAUTENBURG
8564.442588	33708.6	26.8	FIES
8566.400806	24939.9	33.5	FIES
8581.364308	24956.5	36.1	FIES
8583.434302	33152.1	32.4	FIES
8587.367559	31681.2	21.5	FIES
8587.474228	30949.2	27.0	FIES
8588.453630	24951.0	45.7	FIES
8589.369006	28516.5	47.5	FIES

$R \approx 44,000$ over the wavelength range of 370–850 nm (Kabáth et al. 2019b, 2020). All spectra have an exposure time of 3600 s resulting in a signal-to-noise (S/N) per pixel at 550 nm varying between 16 and 22, depending on the observing conditions and the airmass. We use the standard IRAF 2.16 routines (Tody 1993) to process the spectra, which were corrected for bias, flat field, and cosmic rays. The spectrum with the highest S/N was used as template for the cross-correlation done with

the IRAF `fxcor` routine, allowing us to remove instrumental shift by measuring the shift in telluric lines, and to measure the relative RVs. The errors are standard deviations of values from eighteen 10 nm intervals that were considered.

2.5.1. FIES Spectra

We acquired 8 spectra with the Fibre-fed Échelle Spectrograph (FIES; Frandsen & Lindberg 1999; Telting et al. 2014) mounted at the 2.56 m Nordic Optical Telescope (NOT) of Roque de los Muchachos Observatory (La Palma, Spain). FIES has a resolving power of $R \approx 47,000$. The observations were carried out between 2019 March 21 and April 15 UT, as part of the observing programs 58-024 and 59-210. The exposure time was set to 1500–2100 s—depending on sky and seeing conditions, leading to a S/N ratio per pixel of ~ 70 –100 at 5500 Å. We followed the observing strategy described in Buchhave et al. (2010) and Gandolfi et al. (2015), and traced the RV drift of the instrument by acquiring long-exposed ThAr spectra ($T_{\text{exp}} \approx 60$ s) immediately before and after each science exposure. We reduced the FIES spectra following standard IRAF and IDL routines and extracted the RV measurements via multi-order cross-correlations with the RV standard star HD 182572 (Udry et al. 1999) observed with the same instrument set-up as TOI-503.

2.5.2. Tautenburg Spectra and Doppler Tomography Analysis

We used the 2 m Alfred Jensch telescope of the Thüringer Landessternwarte Tautenburg to obtain 28 spectra of TOI-503. The telescope is equipped with an echelle spectrograph with spectral resolving power $R \approx 35,000$ with the 2'' slit used. The spectra used for orbital analysis have an exposure time 1200 s, resulting in an S/N ratio between 23 and 27. We processed the spectra using the Tautenburg Spectroscopy pipeline (Sabotta et al. 2019) built upon PyRaf and the Cosmic Ray code by Malte Tewes based on the method by van Dokkum (2001). We use cross-correlation routines from IRAF to correct spectra for the shift in telluric lines and to measure the relative RVs. There are 17 spectra from the 28 that have an exposure time of 600 s and that were taken in an attempt to extract a Doppler tomography (DT; e.g., Hatzes 1998; Albrecht et al. 2007; Collier Cameron et al. 2010a) signal during the transit night of 2019 April 17. These are not used for the RV measurements to avoid the signal created by the BD blocking light from the host star, which creates an additional Doppler shift that is based on the orbital alignment and rotation rate of the star, and not the orbital motion of the BD.

The DT technique reveals the distortion of the stellar line profiles when a planet or BD blocks part of the stellar photosphere during a transit. This distortion is a tiny bump in the stellar absorption profile, scaled down in width according to the BD-to-star radius ratio. Additionally, the area of that bump corresponds to the BD-to-stellar disks area ratio. As the BD moves across the stellar disk, the bump produces a trace in the time series of line profiles, which reveals the spin-orbit alignment between the star and BD orbit. For this analysis, we first created a reference stellar absorption spectrum consisting of delta functions at the wavelength positions of the observed stellar absorption lines. Their positions and strengths were determined by fitting each stellar absorption line in the observed spectrum with the rotational profile of TOI-503 ($v \sin i = 26$ km s^{−1}). A total of 410 stellar absorption lines

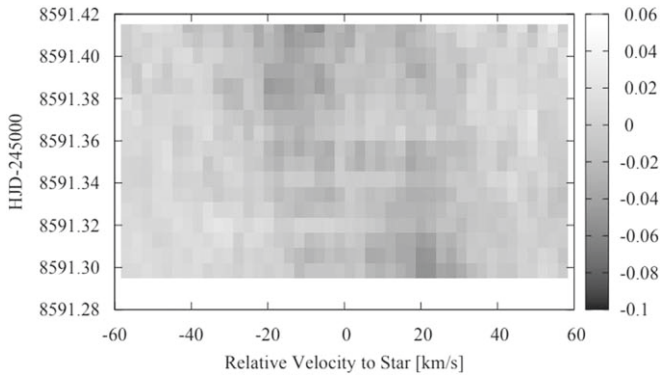


Figure 3. Doppler tomography using Tautenburg in-transit spectra.

were identified in the wavelength range from 455.8 to 674.6 nm. We excluded those wavelength regions from our analysis which exhibited telluric lines, the Hydrogen Balmer absorption lines, and the Na II doublet around 589 nm.

By employing a least-squares deconvolution similar to what is shown in Collier Cameron et al. (2002) of the observed spectra with the reference spectrum, we summed up the 410 stellar absorption lines in each spectrum into one high S/N mean line profile. The resulting line profiles were scaled so that their height was one, and were interpolated onto a velocity grid of 2.65 km s^{-1} increments, corresponding to the velocity range of one spectral pixel at 550 nm. We then summed up all the mean line profiles collected the nights before the transit and subtracted the resulting profile from the in-transit ones. Figure 3 shows the residuals of the line profiles and shows that we are unable to detect a trace of the transiting planet using this method.

2.6. TRES Spectra

We used the Tillinghast Reflector Echelle Spectrograph (TRES) on Mount Hopkins, Arizona, to obtain spectra of TOI-503 between 2019 March 23 and April 14. The spectrograph has a resolving power of $R \approx 44,000$ and covers wavelengths from 390 to 910 nm. Forty-three spectra of TOI-503 were taken with TRES with exposure times ranging from 195 to 300 s and S/N ranging from 35 to 59. The relative RVs that we derive from TRES spectra use multiple echelle orders from each spectrum that are cross-correlated with the highest S/N spectrum of the target star. We omit individual orders with poor S/N and manually remove obvious cosmic rays. Of these 43 spectra, 33 were taken in an attempt to extract a DT signal, but as with our analysis of the Tautenburg in-transit DT spectra, we do not find a noticeable signal.

2.7. PARAS Spectra

We obtained seven spectra with the PARAS spectrograph (Chakraborty et al. 2014) coupled with the 1.2 m telescope at Gurushikhar Observatory, Mount Abu, India, between 2019 April 6 and 11 at a resolving power of $R \approx 67,000$, in the wavelength range of 380–690 nm. Each night had a median seeing of around $1''.5$. The exposure time for each measurement was kept at 1800 s, which resulted in a S/N of 20–25 at the blaze peak wavelength of 550 nm. The spectra were extracted using a custom-designed automated pipeline written in IDL, based on the algorithms of Piskunov & Valenti (2002). The extracted spectra were cross-correlated with the template spectrum of an A-type star to calculate the relative RVs. Further details of

the spectrograph and data-analysis procedure can be found in Chakraborty et al. (2014). The uncertainties reported here are the cross-correlation function fitting errors combined with the photon noise in the same way as described in Chaturvedi et al. (2016, 2018).

3. Analysis

3.1. Modeling Stellar Parameters

We use *iSpec* (Blanco-Cuaresma et al. 2014; Blanco-Cuaresma 2019) and the Stellar Parameter Classification (SPC) software Buchhave et al. (2012) to analyze the spectra of TOI-503. Then, with the spectral properties as well as an SED, a light curve, and a *Gaia* parallax of the star, we use EXOFASTv2 (Eastman et al. 2019), and a combination of PARAM 1.3 (to model the stellar parameters; da Silva et al. 2006), GeePea (to model the light curve; Gibson et al. 2012), and Systemic Console (to model the RV curve; Meschiari et al. 2009), to independently model the star and BD.

3.1.1. *iSpec* Stellar Parameters

We use *iSpec* to perform a detailed analysis of the host star from the FIES spectra. Specifically, we use the Synthe radiative transfer code (Kurucz 1993), the MARCS atmosphere models (Gustafsson et al. 2008), and version 5 of the GES atomic line list (Heiter et al. 2015) between 420 and 920 nm, which includes 35 different chemical species. These are incorporated into the framework of *iSpec*. We co-add all the eight FIES spectra (after the RV shift correction) to increase the S/N and use them to determine the effective temperature T_{eff} , metallicity [Fe/H], surface gravity $\log g$, and the projected stellar equatorial velocity $v \sin i$. We model the stellar parameters using the Bayesian parameter estimation code PARAM 1.3 and use the parallax measured by *Gaia* DR2 ($\varpi = 3.8875 \pm 0.0591$ mas; Lindegren et al. 2018) for the distance of the star and Tycho V magnitude (Høg et al. 2000). PARAM 1.3 code estimates stellar properties using the PARSEC isochrones (Bressan et al. 2012). We calculate the value of $\log g$ iteratively to ensure an agreement between *iSpec* and PARAM 1.3. We determine the effective temperature by fitting the $H\alpha$ Balmer line (Cayrel et al. 2011), and the metallicity by fitting for 22 Fe I lines in the interval 597–643 nm. From this analysis, we find TOI-503 to be a metallic-line A star, or Am star, with a metallicity of $[\text{Fe}/\text{H}] = 0.61 \pm 0.07$.

The formation of Am stars is generally attributed to the slowing of the stellar rotation via tidal force caused by a binary star (Michaud et al. 1983). Am stars are generally slow rotators compared to typical A stars, with rotation rates below 120 km s^{-1} (Abt & Morrell 1995). The study by Abt & Moyn (1973) suggests that all slowly rotating A-type main-sequence stars are chemically peculiar (i.e., those with high iron abundance or unusual depletion of key elements such as Ca). The rotation period of TOI-503 ($P_{\text{rot}} = 3.64$ days) is determined from the projected stellar equatorial velocity, the inclination derived from GeePea, and the radius of the star derived from PARAM 1.3. The rotation period of the star is similar to the orbital period of the BD ($P_{\text{orb}} = 3.67$ days), which is indicative of synchronism. This analysis assumes the alignment between the equatorial and orbital planes of the star. However, such an assumption is not surprising for the close binary system like TOI-503. For example, the paper by Hale (1994) suggests approximate alignment for solar-type binaries under the separation of 30–40 au. The paper by Hut (1980)

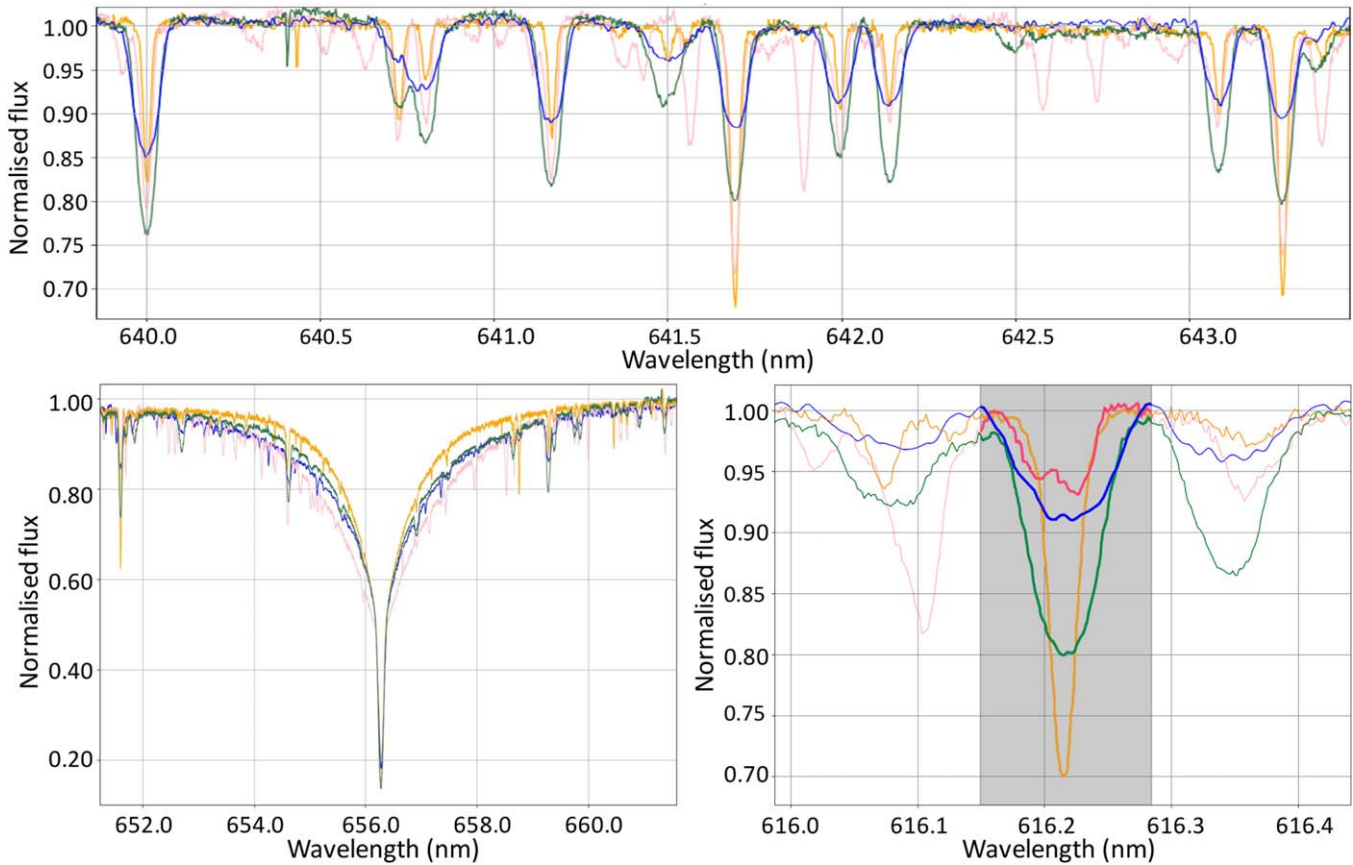


Figure 4. Spectrum of TOI-503 (blue line) and three templates with similar temperatures (Am-star template—green line, A-star template—orange line, Ap-star template—pink line), over-plotted for comparison. Top: iron lines region. Bottom left: the $H\alpha$ Balmer line. Bottom right: a Ca I line highlighted by gray region.

shows that for close binary systems where the tidal evolution is the primary mechanism linked with temporal changes in orbital parameters, the tidal equilibrium can be established only under assumptions of coplanarity, circularity, and synchronized rotation. Furthermore, the similarity with the rotation period determined from the photometric light curve in Section 3.1.4 also reflects approximate alignment. Such a slow rotation rate would enable the onset of radiative diffusion within the stable atmosphere, which leads to the abundance of elements observed in the spectrum, as in Am stars (Michaud et al. 1983). In this context, comparing the TOI-503 spectrum with the templates of a normal A-type star, a magnetically peculiar Ap star, and an Am star from the ESO database⁵⁴ reveals the clear similarity between the observed spectrum of TOI-503 and that of the Am stars (Figure 4). However, the most persuasive argument would be that the overabundance (in context of A-type stars) of the iron group elements is coupled with an underabundance of key light elements, such as Ca, Sc, or Mg, which is the characteristic sign of Am stars. The abundances we derive point to this conclusion precisely, thereby confirming the Am classification. The stellar parameters and the abundances of selected species are reported in Table 3.

3.1.2. Stellar Parameter Classification and EXOFASTv2 Modeling

We also use SPC with the TRES spectra to independently (from iSpec and FIES) derive effective temperature (T_{eff}),

metallicity ($[\text{Fe}/\text{H}]$), surface gravity ($\log g$), and the projected stellar equatorial velocity ($v \sin i$) for TOI-503. We iteratively use SPC with EXOFASTv2 (Eastman et al. 2019) to determine values for T_{eff} and $[\text{Fe}/\text{H}]$, meaning that we use the $\log g$ from EXOFASTv2 as a fixed parameter in SPC and then take the T_{eff} and $[\text{Fe}/\text{H}]$ from SPC (with the fixed $\log g$ from EXOFASTv2) as starting values in a new EXOFASTv2 analysis. However, due to the upper limit of $[\text{Fe}/\text{H}] \leq +0.5$ for the metallicity of the MIST isochrones (Paxton et al. 2015; Choi et al. 2016; Dotter 2016) that EXOFASTv2 utilizes, we rely on our measurements using iSpec for the metallicity. With SPC, we measure a metallicity of $[\text{Fe}/\text{H}] = 0.34 \pm 0.08$ with a fixed $\log g = 4.23$ from an initial EXOFASTv2 analysis. The parameters T_{eff} , $[\text{Fe}/\text{H}]$, and $\log g$ are not fixed in subsequent EXOFASTv2 analyses, and only $\log g$ is fixed in subsequent SPC analyses. The $[\text{Fe}/\text{H}]$ value is about 0.27 dex lower than our value from iSpec, most likely because SPC explicitly measures $[\text{m}/\text{H}]$, which is a good approximation for $[\text{Fe}/\text{H}]$, assuming a Solar-like composition and chemical proportions (not the case for TOI-503). We use SPC on a co-added spectrum with the RV shifts corrected for. We do not co-add any spectrum with $\text{S/N} < 15$. With SPC, we use the 503–532 nm wavelength range (centered on the Mg b triplet) on a single co-added TRES spectrum.

We derive the mass and radius of the BD using EXOFASTv2, which uses the Monte Carlo-Markov Chain (MCMC) method. For each MCMC fit, we use $N = 36$ ($N = 2 \times n_{\text{parameters}}$) walkers, or chains, and run for 50,000 steps, or links. We modeled the host star mass and radius using

⁵⁴ http://www.eso.org/sci/observing/tools/uvespop/field_stars_uptonow.html

Table 3
Comparison of Parameters between Analysis Methods

Parameter	SPC/EXOFASTv2	iSpec/PARAM 1.3
M_* (M_\odot)	1.80 ± 0.06	1.78 ± 0.02
R_* (R_\odot)	1.70 ± 0.05	1.77 ± 0.04
$\log g$	4.23 ± 0.03	4.17 ± 0.02
T_{eff} (K)	7650 ± 160	7639 ± 105
[Fe/H]	0.30 ± 0.09	0.61 ± 0.07
[Ni/H]	...	0.58 ± 0.09
[Ca/H]	...	-0.40 ± 0.11
[Sc/H]	...	0.10 ± 0.14
[Mg/H]	...	0.25 ± 0.15
$v_{\text{rot}} \sin i_*$ (km s^{-1})	28.6 ± 0.4	25.0 ± 0.3
P_{rot} (days)	3.01 ± 0.09	3.64 ± 0.13
Age (Gyr)	$0.18^{+0.17}_{-0.11}$	0.14 ± 0.04
Parameter	EXOFASTv2	GeePea/Systemic Console
M_b (M_J)	53.7 ± 1.2	53.3 ± 1.1
R_b (R_J)	1.34 ± 0.26	1.28 ± 0.29
$R_{b,\text{mode}}$ (R_J)	1.27 ± 0.15	...
Period (days)	3.6772 ± 0.0001	3.6775 ± 0.0002
a/R_*	7.22 ± 0.22	7.47 ± 0.19
R_b/R_*	0.0805 ± 0.015	0.0724 ± 0.015
b	0.974 ± 0.022	0.956 ± 0.023
Inclination i (degree)	82.25 ± 0.41	82.65 ± 0.38
e	0 (adopted)	0 (adopted)

Note. The parameters here are the median values except for the EXOFASTv2 R_p , which shows both the median and the mode.

the MIST isochrones, which are integrated into the framework of EXOFASTv2. Figure 5 shows the orbital solution we derive with EXOFASTv2 with a joint fit of the RV and transit data. Our transit solution from this same joint fit agrees with that shown via the GeePea analysis (Figure 6). We account for interstellar extinction, A_V , using the Galactic dust and reddening extinction tool from IRAS and COBE/DIRBE,⁵⁵ and take this value of $A_V = 0.0791$ as an upper limit for our priors in EXOFASTv2. We also use the parallax of TOI-503 as measured by *Gaia* DR2 and the SPC results for T_{eff} and metallicity ([Fe/H] = 0.34) as starting points for our priors. The full list of free parameters we specify for each object is period P , time of conjunction (T_C in BJD), host star effective temperature T_{eff} , host star metallicity [Fe/H], RV semi-amplitude K , RV relative offset to the systemic velocity γ_{rel} , interstellar extinction A_V , parallax, orbital inclination i , and R_b/R_* . We initially allow the eccentricity e to be a free parameter and find it to be close to zero at $e \approx 0.007 \pm 0.003$ ($e \cos \omega = -0.0058 \pm 0.0032$, $e \sin \omega = -0.0004 \pm 0.0037$). In order to avoid the Lucy–Sweeney bias (Lucy & Sweeney 1971), we fix the eccentricity to zero in all subsequent analyses. The derived T_{eff} from EXOFASTv2 agrees well with the spectroscopic T_{eff} from SPC. We impose Gaussian priors on these free parameters in EXOFASTv2. The median value with 1σ uncertainties of the MCMC chains for each parameter is reported in Table 4. The parameters derived from EXOFASTv2 are consistent with those derived from our other independent analyses.

⁵⁵ Galactic dust and reddening extinction tool: <https://irsa.ipac.caltech.edu/applications/DUST/>.

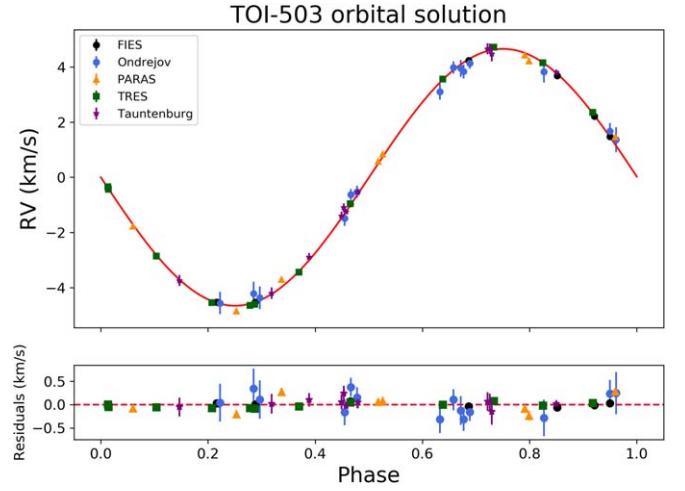


Figure 5. Orbital solution for TOI-503 showing the EXOFASTv2 RV model in red. This orbital solution is jointly derived by simultaneously fitting all RVs from the different contributing spectrographs and the normalized PDCSAP TESS light curve.

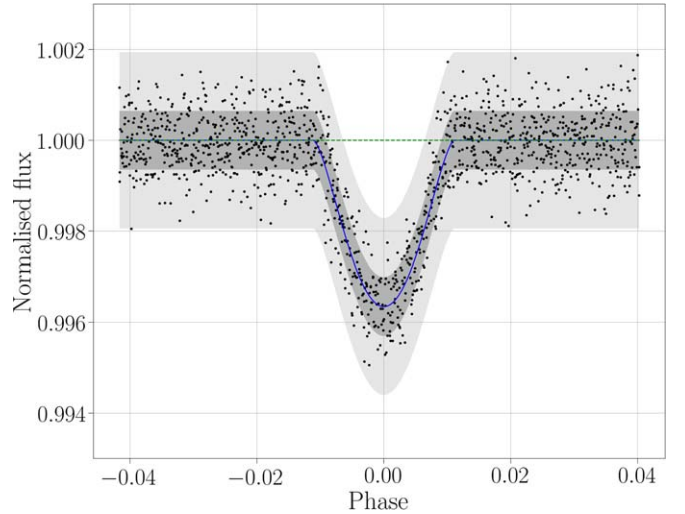


Figure 6. Transit light curve of the TOI-503, fitted with the GP model described in Section 3.1.3. The blue line represents the best fitting transit light curve, and the green line shows the model without the transit function. The dark and light gray regions represent the 1σ and 3σ prediction of the GP model.

3.1.3. Systemic Console and GeePea Modeling

Besides EXOFASTv2, we also use the Systemic Console package to model the orbital solution additionally. We consider data from each spectrograph with corresponding velocity offsets to be free parameters allowing us to fit all data sets simultaneously. By synergy of the Lomb–Scargle (LS) periodogram and Levenberg–Marquardt minimization method, we found the best solution providing the starting values for an MCMC analysis with four chains with 1000 walkers of 50,000 iterations. As the SPOC LC gives us a better estimate of the orbital period, we fix this value in all analyses. Similarly to EXOFASTv2 modeling, we also fix the eccentricity to zero to avoid the Lucy–Sweeney bias. The median values of the main parameters with 1σ uncertainties of the MCMC chains, together with values from EXOFASTv2 modeling, are reported in Table 3. The parameters derived from the Systemic Console are consistent with those derived from our other independent analyses.

Table 4
Median Values and 68% Confidence Interval for TOI-503, Created Using EXOFASTv2 Commit Number 65aa674

Parameter	Units	Values				
Stellar Parameters:						
M_*	Mass (M_\odot)	$1.80^{+0.06}_{-0.06}$				
R_*	Radius (R_\odot)	$1.70^{+0.05}_{-0.04}$				
L_*	Luminosity (L_\odot)	$8.96^{+0.54}_{-0.54}$				
ρ_*	Density (cgs)	$0.51^{+0.04}_{-0.05}$				
$\log g$	Surface gravity (cgs)	$4.23^{+0.03}_{-0.03}$				
T_{eff}	Effective temperature (K)	7650^{+140}_{-160}				
[Fe/H]	Metallicity (dex)	$0.30^{+0.08}_{-0.09}$				
Age	Age (Gyr)	$0.18^{+0.17}_{-0.11}$				
EEP	Equal evolutionary point	292^{+22}_{-31}				
A_V	V-band extinction (mag)	$0.038^{+0.028}_{-0.026}$				
σ_{SED}	SED photometry error scaling	$3.9^{+1.7}_{-0.99}$				
ϖ	Parallax (mas)	$3.878^{+0.059}_{-0.058}$				
d	Distance (pc)	$257.9^{+3.9}_{-3.8}$				
Brown-dwarf Parameters:						
		b				
P	Period (days)	3.67718 ± 0.00010				
R_b	Radius (R_J)	$1.34^{+0.26}_{-0.15}$				
T_C	Time of conjunction (BJD _{TDB})	$2458492.05383 \pm 0.00053$				
T_0	Optimal conjunction time (BJD _{TDB})	$2458506.76256 \pm 0.00039$				
a	Semimajor axis (au)	0.05727 ± 0.00063				
i	Inclination (Degrees)	$82.25^{+0.31}_{-0.41}$				
T_{eq}	Equilibrium temperature (K)	2011^{+27}_{-28}				
M_b	Mass (M_J)	53.7 ± 1.2				
K	RV semi-amplitude (m s ⁻¹)	4640^{+30}_{-27}				
$\log K$	Log of RV semi-amplitude	$3.6673^{+0.0028}_{-0.0026}$				
R_b/R_*	Radius of planet in stellar radii	$0.0805^{+0.015}_{-0.0090}$				
a/R_*	Semimajor axis in stellar radii	$7.22^{+0.20}_{-0.22}$				
δ	Transit depth (fraction)	$0.0065^{+0.0028}_{-0.0014}$				
Depth	Flux decrement at mid transit	$0.00452^{+0.00026}_{-0.00023}$				
τ	Ingress/egress transit duration (days)	$0.03836^{+0.00060}_{-0.00057}$				
T_{14}	Total transit duration (days)	$0.0767^{+0.0012}_{-0.0011}$				
b	Transit impact parameter	$0.974^{+0.022}_{-0.015}$				
$\delta_{S,3.6 \mu\text{m}}$	Blackbody eclipse depth at 3.6 μm (ppm)	700^{+320}_{-160}				
$\delta_{S,4.5 \mu\text{m}}$	Blackbody eclipse depth at 4.5 μm (ppm)	860^{+390}_{-200}				
ρ_b	Density (cgs)	27^{+13}_{-11}				
$\log g_P$	Surface gravity	$4.87^{+0.12}_{-0.17}$				
$M_P \sin i$	Minimum mass (M_J)	53.2 ± 1.2				
M_P/M_*	Mass ratio	$0.02844^{+0.00039}_{-0.00037}$				
c_1	Linear limb-darkening coeff	$0.146^{+0.049}_{-0.050}$				
c_2	Quadratic limb-darkening coeff	$0.333^{+0.049}_{-0.048}$				
Telescope Parameters:		FIES	Ondřejov	PARAS	TRES	Tautenburg
γ_{rel}	Relative RV offset (m s ⁻¹)	29468^{+22}_{-20}	3549^{+77}_{-78}	-31^{+85}_{-84}	4571^{+21}_{-23}	-2766^{+43}_{-35}
σ_1	RV jitter (m s ⁻¹)	46^{+41}_{-30}	120 ± 120	230^{+100}_{-66}	40^{+43}_{-40}	$0.00^{+93}_{-0.00}$
σ_1^2	RV jitter variance	2200^{+5500}_{-1900}	13000^{+40000}_{-22000}	53000^{+57000}_{-26000}	1600^{+5300}_{-2200}	-1800^{+11000}_{-3500}
Transit Parameters:		TESS UT oi50-3.-TE (TESS)				
σ^2	Added variance	$-0.0000000323^{+0.0000000064}_{-0.0000000063}$				
F_0	Baseline flux	0.9999834 ± 0.0000059				

TOI-503 has a V-shaped, grazing transit. In general, V-shaped eclipses are often considered false positives caused by binary stars with similar radii, stellar grazing eclipses, or a blended eclipsing binary, such as a background binary or one bound to the target star in a triple system. In this case, we ruled out the possibility of a false-positive scenario with a combination of follow-up RVs to determine the mass of the companion and high-resolution imaging to rule out a blend. This implies a rather low inclination in context of BDs that we measure to be roughly $i = 82^\circ.25 \pm 0.41$ or an impact

parameter of $b = 0.974^{+0.022}_{-0.015}$. There are slightly more than 10 similar systems known (Alsubai et al. 2018), but only one that includes a BD (Csizmadia et al. 2015). The analysis of grazing eclipses is rather challenging and often degenerate between the radius of the transiting object and its impact parameter b .

We fit the light curve using the GeePea code, which is based on Gaussian processes (GPs) and described by Gibson et al. (2012). We use square exponential kernel function and assume uniform, uninformative priors for all the parameters of the transit and noise model with the additional restrictions for

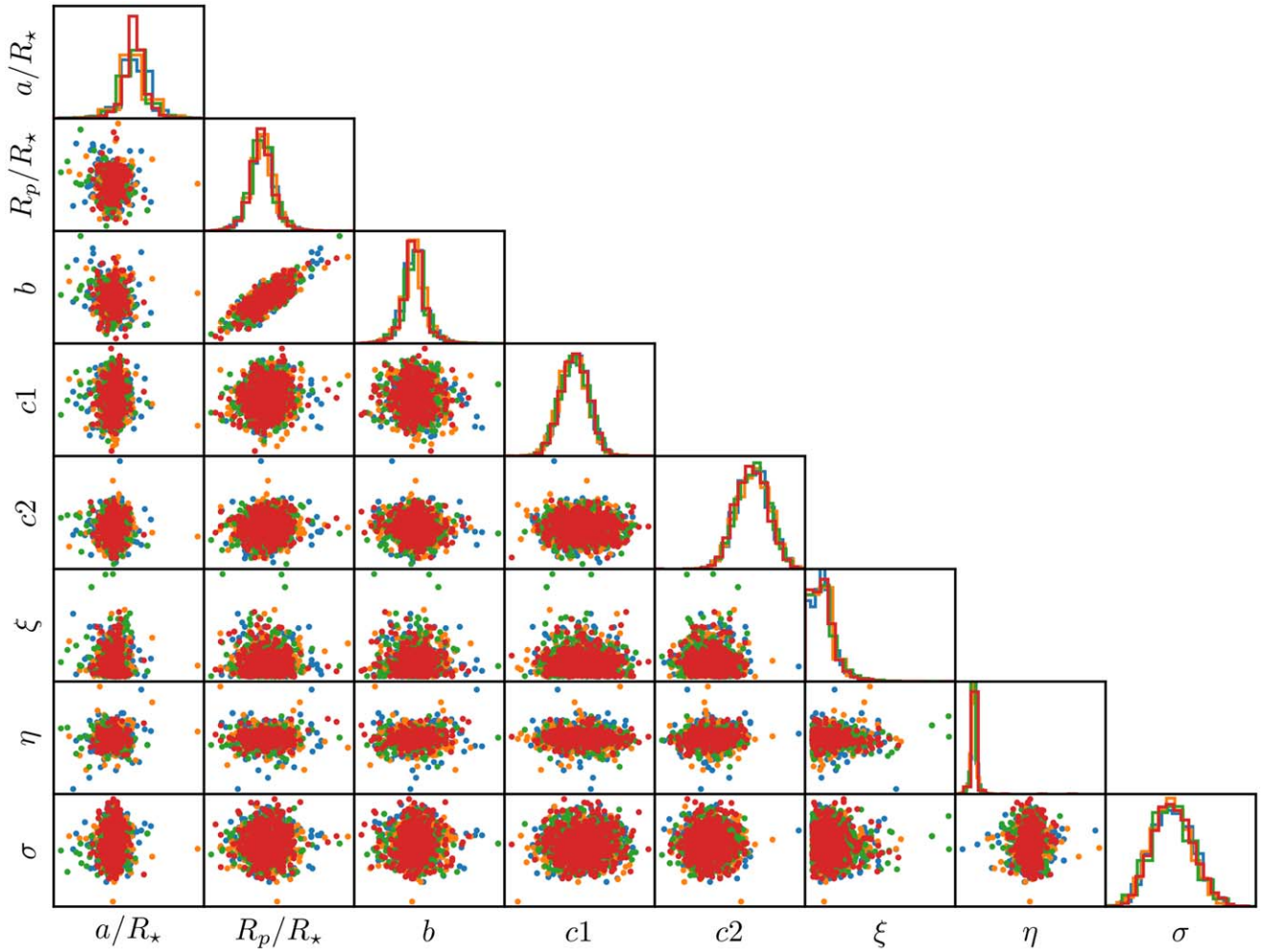


Figure 7. Correlations between the free parameters of the LC model from the MCMC analysis using the *GeePea* code. At the end of each row is shown the derived posterior probability distribution. We use the quadratic limb-darkening law with the coefficients c_1 and c_2 . ξ (output scale describing the GP’s variance), η (length scale that determines smoothness of the function), and σ (Poisson noise) are the parameters of the noise model. The four different colors represent samples from the independent MCMC chains.

the limb-darkening coefficients chosen so as to ensure a positive surface brightness, and for all hyper-parameters of the noise model chosen such as to ensure their values are positive. Since limb darkening, radius ratio, and impact parameter are degenerate here due to the grazing transit geometry, the fitted values for the radius ratio and impact parameter dominate the limb-darkening measurement. Considering this, we set Gaussian priors on the limb-darkening coefficients obtained from the tables of Claret (2017). The fit of the light curve is presented in Figure 6. We use the MCMC method with four chains with 1000 walkers of 40,000 iterations to find out the uncertainties for the each parameter of the transit and noise model. Plots of posterior distributions and correlation plots are presented in Figure 7. The determined values for the parameters are summarized in Table 3 and are found independently from those found using EXOFASTv2.

We also use other analysis tools to perform independent analyses of the RV and transit data and derive the stellar and the BD parameters of TOI-503: PYANETI (Barragán et al. 2019) and MISTTBORN⁵⁶ (Mann et al. 2016; Johnson et al. 2018). All the

codes converge to a consistent solution for the stellar and BD parameters.

3.1.4. Analysing the Surface Rotation

Even though it is not completely clear that A-type stars have spots, there are a variety of studies on the discovery of spots on the well-known star Vega (Balona 2017; Böhm et al. 2015; Petit et al. 2017) and more studies about the measurement of the rotation based on spot modulation for A-type stars (Balona 2011, 2013). There is even previous evidence of the detectable presence of spots on Am-type stars (Balona et al. 2015). Thus it is reasonable to search for the signature of the rotation period through the modulation caused by the star spots in TOI-503. To do this, we use the SPOC two-minute cadence light curve of TOI-503. We removed the signal of the primary and secondary transits using the known ephemerides and then filled all gaps, including the transits and the data-transfer gaps, using in-painting techniques based on a multi-scale discrete cosine transform as described in García et al. (2014b) and Pires et al. (2015).

We then search for modulation in the resulting light curve by performing the following steps. First, we perform a

⁵⁶ <https://github.com/captain-exoplanet/misttborn>

time-frequency analysis based on wavelets decomposition (Torrence & Compo 1998; Mathur et al. 2010; García et al. 2014a) to compute the wavelet power spectrum (WPS), which we subsequently project on the period axis to form the global wavelets power spectrum (GWPS). In the second step, we perform auto-correlation function analysis (ACF, McQuillan et al. 2014) to extract the most significant signal, which corresponds to a particular period. Finally, by a combination of previous two steps (specifically multiplying them), we create a function called the composite spectrum (CS; Ceillier et al. 2016, 2017). As these steps are sensitive to different types of artifacts in a light curve, by deriving the CS, we can mask such artifacts and highlight a periodic signal created by stellar activity such as star spots. The pipeline that combines these different techniques has been applied to simulated data (Aigrain et al. 2015) and has been already performed to a large number of solar-like stars and red giants (e.g., Santos et al. 2019) with reliable success.

The original light-curve analysis with the transits provides a period of $P_{\text{GWPS}} = 3.66$ days, corresponding to the orbital period of the BD. Once the transits are removed, we find a period of $P_{\text{GWPS}} = 3.24$ days with the wavelet analysis and $P_{\text{ACF}} = 3.55$ days with the ACF analysis. The height of the peak in the ACF (H_{ACF} , measured from the maximum to the adjacent minima) is 0.5, which fulfills our criteria for a reliable result ($H_{\text{ACF} > 0.4}$). We note that we detect the overtone of half of the real rotation period $P_{\text{GWPS}} = 1.8$ days using wavelets decomposition analysis, which can be seen in Figure 8. This period is detected in power spectra quite often and happens when we observe active regions on the visible side of the star and diametrically opposite side of the star. This period is absent in the CS power spectrum and reveals the final period of $P_{\text{CS}} = 3.50 \pm 0.12$ days. These results are slightly lower than the BD orbital period, but still quite close to it. The rotation period found (Table 3) also agrees with the values obtained spectroscopically from the *iSpec* and *SPC* analyses.

However, given the close values of the rotation period with the orbital period, we cannot completely rule out that the modulation we measure is affected by the orbital motion of the BD. Such an effect would project to LC in the form of additional signals, which are the ellipsoidal deformation signal on the primary star, and the optical reflection plus thermal phase curve signal. We try to distinguish these signals to find the real rotation period. To do so, we apply LS periodograms to the SPOC LC and fit the most significant periods by using the Levenberg–Marquardt minimization method. In Figure 9 we provide the ellipsoidal deformation signal with a period of half of the orbital period with maxima corresponding to phases 0.25 and 0.75 and rotational signal with a period of 3.3 days. We are not able to see any other signals in the LC. That is possibly linked with the nature of this BD. However, future investigation is needed to find an answer.

3.1.5. Stellar Parameters from Gaia DR2

As an additional independent check on the derived stellar parameters, we performed an analysis of the broadband spectral energy distribution (SED) together with the *Gaia* DR2 parallax in order to determine an empirical measurement of the stellar radius, following the procedures described in Stassun & Torres (2016) and Stassun et al. (2017, 2018a). We pulled the $B_T V_T$ magnitudes from *Tycho-2*, the Strömgren *ubvy* magnitudes from Paunzen (2015), the *BVgri* magnitudes from APASS, the

JHK_S magnitudes from 2MASS, the *W1–W4* magnitudes from *WISE*, and the *G* magnitude from *Gaia*. We also used the *GALEX* NUV and/or FUV fluxes, which are available in this case. Together, the available photometry spans the full stellar SED over the wavelength range 0.35–22 μm , and extends down to 0.15 μm when *GALEX* data are available (see Figure 10). We performed a fit using Kurucz stellar atmosphere models, with the priors on effective temperature (T_{eff}), surface gravity ($\log g$), and metallicity ($[\text{Fe}/\text{H}]$) from the spectroscopically determined values. The remaining free parameter is the extinction (A_V), which we restricted to the maximum line-of-sight value from the dust maps of Schlegel et al. (1998).

The resulting fit is very good (Figure 10), with a reduced χ^2 of 4.8. The best-fit extinction is $A_V = 0.00^{+0.06}_{-0.00}$, which is consistent with what we find with EXOFASTv2 ($A_V = 0.038^{+0.028}_{-0.026}$). This zero extinction is consistent with the maximum line-of-sight extinction from the one-dimensional dust maps from Schlegel et al. (1998) of 0.09 mag, as well as the $A_V = 0.12 \pm 0.06$ value from Amôres & Lépine (2005). Integrating the (unreddened) model SED gives the bolometric flux at Earth of $F_{\text{bol}} = 4.18 \pm 0.15 \times 10^{-9} \text{ erg s cm}^{-2}$. Taking the F_{bol} and T_{eff} together with the *Gaia* DR2 parallax, adjusted by +0.08 mas to account for the systematic offset reported by Stassun & Torres (2018), gives the stellar radius as $R = 1.66 \pm 0.05 R_{\odot}$. We note that when we do not account for this systematic offset (as with our values in Table 3 and Figure 11), we measure roughly 2.3% larger radii for the star and BD. This difference does not affect our final conclusions about this system. Finally, estimating the stellar mass from the empirical relations of Torres et al. (2010) gives $M = 1.90 \pm 0.11 M_{\odot}$, which with the radius gives the density $\rho = 0.58 \pm 0.06 \text{ g cm}^{-3}$. We find that this independent check on the stellar mass and radius agrees with the values shown in Table 3.

3.2. Estimating the Age of the TOI-503 System

We report an age of 180^{+170}_{-110} Myr for TOI-503 using the MIST models and EXOFASTv2. We find this consistent with the Yonsei-Yale (YY) isochrone models (Spada et al. 2013), from which we report an age of 200^{+200}_{-130} Myr. Both the MIST and YY isochrone grids are incorporated into the framework of EXOFASTv2. A stellar mass track is interpolated from the grids for the MIST or YY isochrones, and from this, an age is estimated (Eastman et al. 2019). We reiterate that the metallicity range of MIST isochrones is $-5.0 \leq [\text{Fe}/\text{H}] \leq 0.5$, which may influence the accuracy of the age estimate, given that we measure a spectroscopic $[\text{Fe}/\text{H}]$ of 0.6 with *iSpec*. The YY isochrones have a metallicity range of $-3.29 \leq [\text{Fe}/\text{H}] \leq 0.78$, which makes this set of isochrones better suited to this system. Still, we find the stellar and BD properties to be consistent between the two isochrone models.

We now look at the Baraffe et al. (2003; COND03) and Saumon & Marley (2008; SM08) substellar evolutionary models to examine how well they serve as predictors of the age of TOI-503b (Figure 11). The COND03 models present evolutionary tracks for irradiated giant planets and BDs, making them useful in the study of short-period BDs. The Saumon & Marley (2008) models include details like metal-rich, metal-poor, and cloudy atmosphere models for low-mass stars and BDs, but do not include the effects of irradiation. However, both the COND03 and SM08 models are limited in their application to TOI-503b. The BD cooling models from Baraffe et al. (2003) indicate that an object with a mass on the

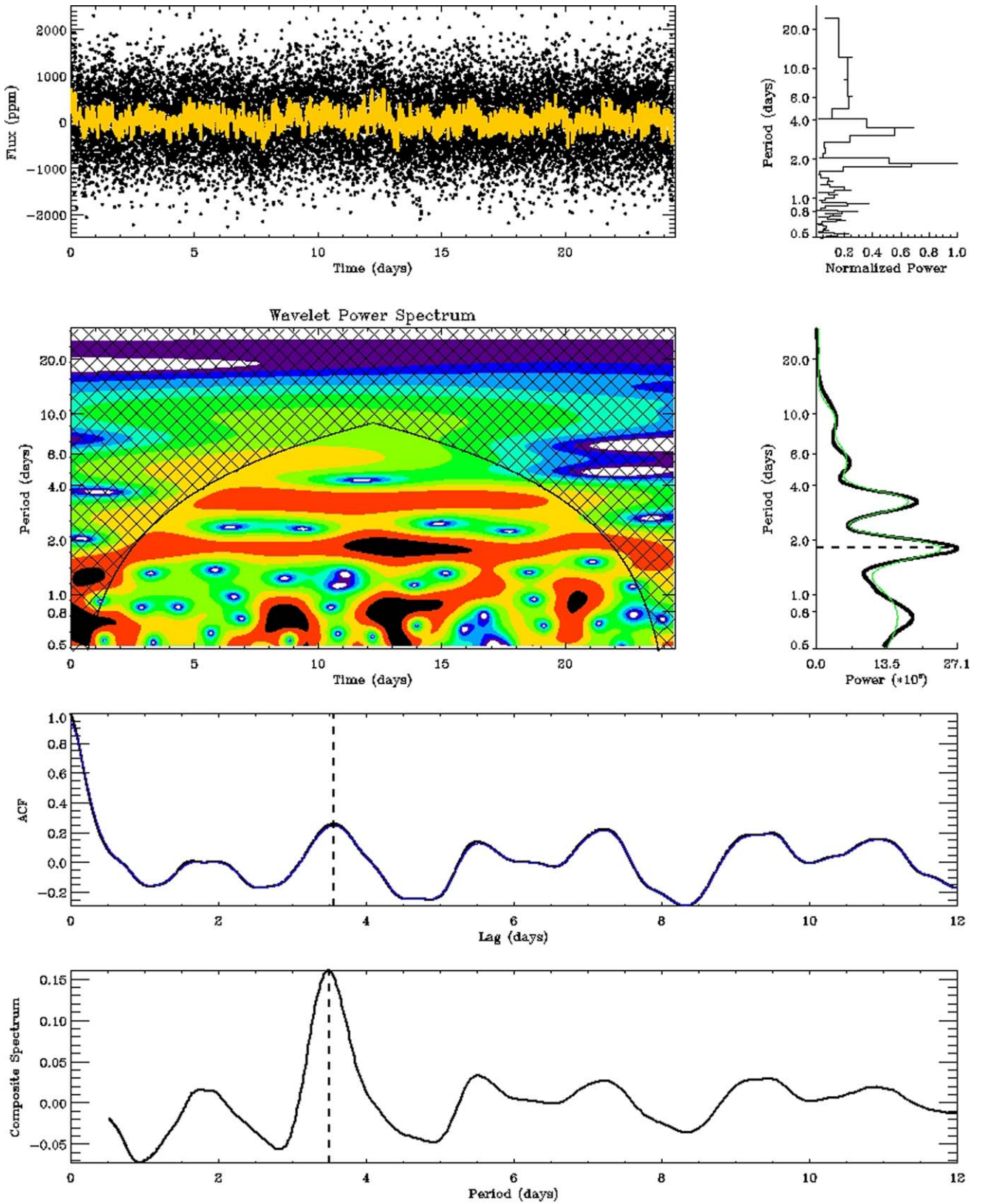


Figure 8. Analysis of modulations in the light curve of TOI-503. Description of the images from top to bottom: First (Left): the light curve cleared for primary and secondary transits. The orange points represent the light curve filtered with a boxcar function of 6 hr width. (Right): LS periodogram with the power normalized to the power of the highest peak. Second (Left): WPS as a function of the period and time. The different colors represent the strength of the power spectrum, where red and dark colors correspond to a higher power, and blue and light colors correspond to lower power. Hatched lines mask the zone of the diagram delimiting the cone of influence—the region where reliable rotation periods can be measured. (Right): GWPS—the projection of the WPS on the Period axis (black line) with the corresponding Gaussian fit (green line). Third: ACF of the light curve. The dashed line points to the selected main periodicity. Fourth: CS of the light curve. The dashed line points to the selected periodicity.

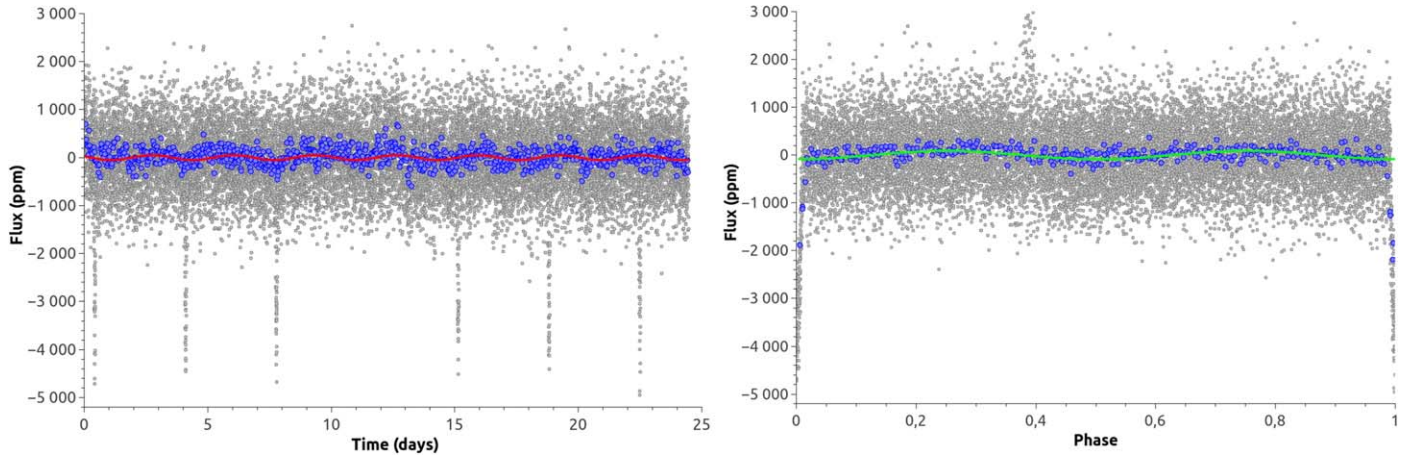


Figure 9. Normalized light curve of TOI-503 observed by *TESS* is plotted in gray with blue points denoting the binned data. The left subplot shows the fit of the rotation signal (red curve), and the right subplot shows the phased data with the fit of the ellipsoidal deformation signal (green curve).

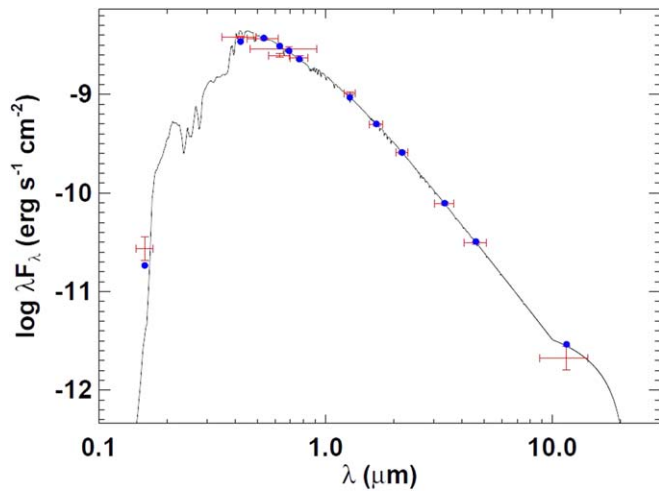


Figure 10. SED fit using *Gaia* DR2 parallax with magnitudes from *Tycho-2* ($B_T V_T$), Paunzen (2015; Strömgren *ubvy*), APASS (*BVgr*), 2MASS (*JHK_s*), WISE (*W1–W4*), and the *G* magnitude from *Gaia*. The SED measurements are in red with the model in blue. The point near 0.15 μm is from *GALEX*.

order of $10M_J$ and an age greater than 500 Myr may maintain a radius of at least $1.0\text{--}1.2 R_J$ while in close proximity (semimajor axis of $a = 0.046$ au) to a host star with $T_{\text{eff}} = 6000$ K. The difference between a non-irradiated and irradiated BD at ages up to 10 Gyr is roughly $0.1R_J$ (Baraffe et al. 2003). However, this is not the most appropriate comparison to TOI-503b, primarily because of the large difference in the mass of the BD in this case ($53M_J$ versus $10M_J$ from the COND03 models), which means that TOI-503b has a higher internal luminosity that will affect its radius over time. We also expect a much hotter star at $T_{\text{eff}} = 7650$ K (versus $T_{\text{eff}} = 6000$ K) to have the effect of slowing the natural contraction of the BD’s radius over time.

Lastly, given the grazing nature of the transit, which limits how well we may constrain the BD radius, we are limited in how thoroughly we may interpret what effects the BD mass and T_{eff} of the host star have on the radius of this substellar companion. This means that the COND03 models may only be used as a broad, qualitative check for the age of TOI-503b. The SM08 models should be treated in a similar, albeit less reliable,

way, as these do not consider the effects of irradiation. However, we are confident that this is one of the youngest intermediate-mass BDs ever found.

4. Discussion

4.1. The Transiting BD Population

The mass–period diagram of transiting BDs (Figure 12) shows a sparse but diverse population. The total number of published transiting BDs, including TOI-503b in this work, is 21 (see Table 5 or Table 6, respectively, for this list). The BD binary system, 2M0535-05 (Stassun et al. 2006), and the very young ($\sim 5\text{--}10$ Myr) RIK 72b, which transits a pre-main-sequence star (David et al. 2019), are not shown in Figure 11 because their radii are above $3R_J$ and do not correspond to the Baraffe et al. (2003) and Saumon & Marley (2008) models, as discussed in Section 3.2. KOI-189b (Díaz et al. 2014) has a mass of $78.0 \pm 3.4M_J$ and is the most massive BD, while HATS-70b, with a mass of $12.9 \pm 1.8M_J$, is the least massive. This neatly places objects at the two extremes in mass of what is considered a BD, but Díaz et al. (2014) caution that KOI-189b may instead be a low-mass star.

TOI-503b has an intermediate-mass of $53.7 \pm 1.2M_J$, an inclination angle of $82.25^{+0.31}_{-0.41}$ degrees ($b = 0.97 \pm 0.02$), and adds to the diversity of objects found in the BD desert, as it is one of the youngest BDs known to transit a main-sequence star. Past works have argued that there is a paucity of objects from $35\text{--}55 M_J \sin i$, $P \leq 100$ days, but this argument is difficult to support given the relatively small number of transiting BDs discovered and the fact that in recent years, five BDs (Gillen et al. 2017; Nowak et al. 2017; Hodžić et al. 2018; Carmichael et al. 2019; Persson et al. 2019, and this work) have been discovered in this intermediate-mass range, bringing new life, so to speak, to the desert. The recent growth in the discoveries of this type of BD could be a hint at an undisclosed population of intermediate-mass BDs in the BD desert. With the rise in the population of BDs in the intermediate-mass range, we cannot rule out further reforestation of the driest region of the BD desert. However, we note that this is mostly a qualitative assessment of the distribution of intermediate-mass BDs, but an interesting feature to highlight nonetheless.

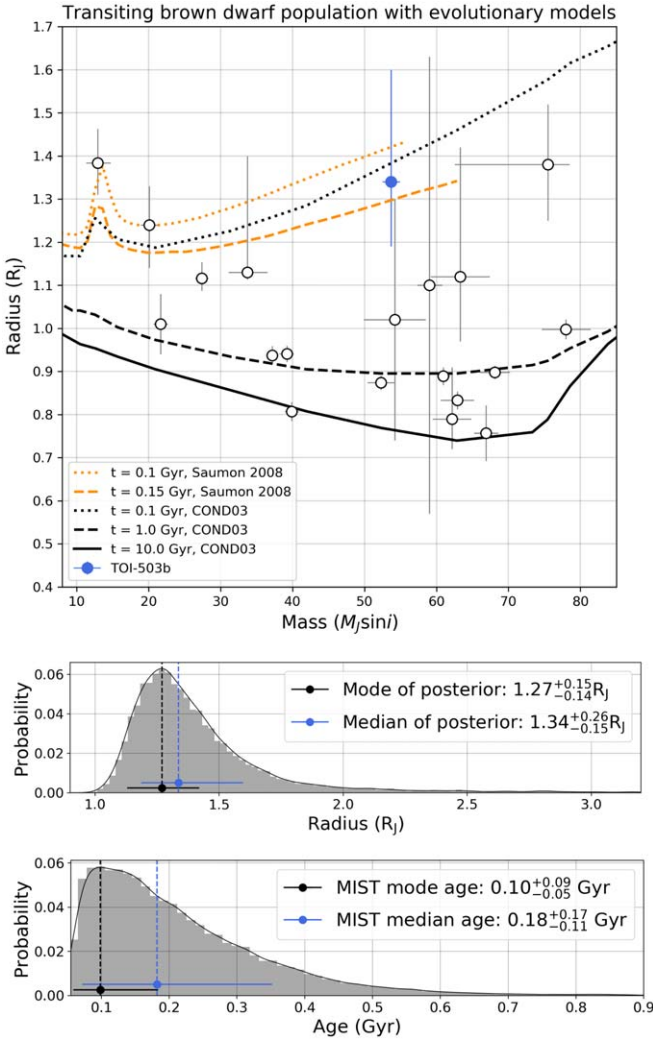


Figure 11. Top: evolutionary brown dwarf models of mass versus radius (Baraffe et al. 2003; Saumon & Marley 2008) with known transiting BDs over-plotted. We use the *median* results from EXOFASTv2 for the mass and radius for TOI-503b in this figure. Middle: posterior distribution of the BD radius from the EXOFASTv2/MIST results for TOI-503. The median value is reported in Table 4 as $1.34^{+0.26}_{-0.15} R_J$, and here, we report a value for the *mode* of the posterior distribution to be $1.30^{+0.15}_{-0.14} R_J$. This is consistent with the posterior distribution for the BD radius using EXOFASTv2/YY. Bottom: the posterior distribution for the age of TOI-503, showing the mode and median values for the age of the system.

4.2. Circularization Timescales and Orbital Synchronization for TOI-503

Based on our estimate of the age of TOI-503 (roughly 180 Myr) and the circular orbit of TOI-503b, we now consider the role tidal interactions have played in the orbital evolution of this system—namely, whether or not tides could have circularized the orbit of the BD. This comparison of circularization timescale to the system’s age has implications for how the BD may have formed.

In order for a binary system affected by tides to be in a stable equilibrium, it must satisfy two conditions: the orbital angular momentum must be at least three times the sum of the rotational angular momenta of the two components, and the total angular momentum of the system must be greater than the

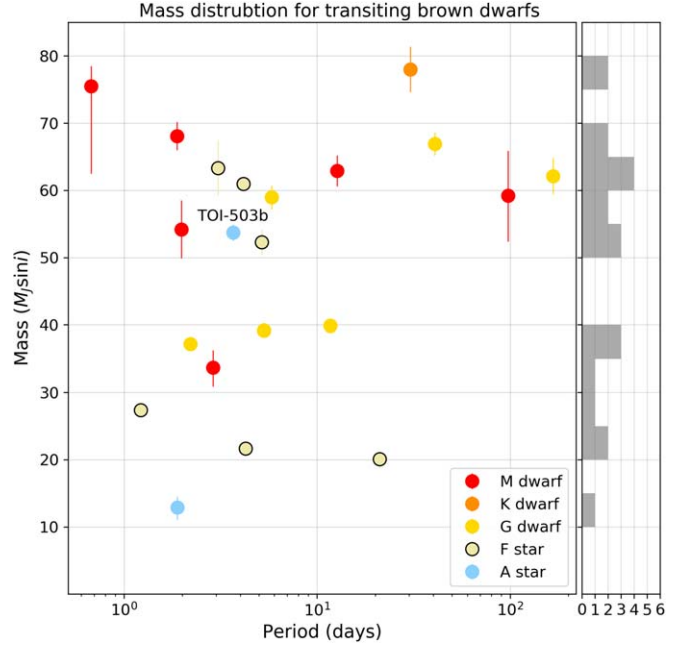


Figure 12. Mass distribution over a period for transiting BDs from Table 5. The color of each point indicates the spectral type of the star that hosts the BD. The histogram of the BD mass distribution is shown in the right panel with bin sizes of $5 M_J$. The absence of BDs in the 40–50 M_J mass range can be seen here, but we caution that this may be a result of the small number of transiting BDs (21) that have been discovered to date.

critical value,

$$L_{\text{crit}} = 4 \left[\frac{G^2}{27} \frac{M_*^3 M_{\text{BD}}^3}{M_* + M_{\text{BD}}} (I_* + I_{\text{BD}}) \right]^{\frac{1}{4}}, \quad (1)$$

where I_* and I_{BD} are the rotational moments of inertia of the star and BD, respectively (Hut 1980). We assume a value of $I_* = \alpha_* M_* R_*^2$ where $\alpha_* = 0.24$, interpolating the stellar moments of inertia from Claret & Gimenez (1989) to the mass of TOI-503. For the BD we assume the same internal structure as Jupiter, such that $\alpha_{\text{BD}} = 0.275$ (Ni 2018). We additionally assume that the orbit of the BD is well-aligned to the stellar rotation (i.e., $\sin i_* \approx 1$), in order to calculate the stellar rotation period from $\nu \sin i_*$, and we assume the present-day stellar rotation rate for the quoted calculations. We find that $L_{\text{tot}} = 1.07 \pm 0.07 L_{\text{crit}}$ and $L_{\text{orb}} = 5.0 \pm 0.5 L_{\text{rot}}$. TOI-503 is thus Darwin stable; interestingly, the total angular momentum is consistent with being equal to the critical value, while the orbital angular momentum is close to twice the critical value relative to the rotational angular momentum, both much like KELT-1b (Siverd et al. 2012).

From Jackson et al. (2008), the timescale for orbital circularization timescale for a close-in companion is

$$\frac{1}{\tau_e} = \left[\frac{63}{4} \sqrt{GM_*^3} \frac{R_{\text{BD}}^5}{Q_{\text{BD}} M_{\text{BD}}} + \frac{171}{16} \sqrt{G/M_*} \frac{R_*^5 M_{\text{BD}}}{Q_*} \right] a^{-\frac{13}{2}}, \quad (2)$$

where Q_* and Q_{BD} are the tidal quality factors of the star and BD, respectively. Jackson et al. (2008) did not provide an expression for the tidal synchronization timescale, but

Table 5
List of Published Transiting Brown Dwarfs as of 2019 June

Name	P (days)	M_{BD}/M_J	R_{BD}/R_J	e	M_*/M_\odot	R_*/R_\odot	T_{eff} (K)	[Fe/H]	Reference
TOI-503b	3.677	53.7 ± 1.2	$1.34^{+0.26}_{-0.15}$	0 (adopted)	1.80 ± 0.06	1.70 ± 0.05	7650 ± 160	$+0.61 \pm 0.07$	this work
HATS-70b	1.888	$12.9^{+1.8}_{-1.6}$	$1.38^{+0.08}_{-0.07}$	<0.18	1.78 ± 0.12	$1.88^{+0.06}_{-0.07}$	7930^{+630}_{-820}	$+0.04 \pm 0.11$	(1)
KELT-1b	1.218	27.4 ± 0.9	1.12 ± 0.04	0.01 ± 0.01	1.34 ± 0.06	1.47 ± 0.05	6516 ± 49	$+0.05 \pm 0.08$	(2)
NLTT 41135b	2.889	33.7 ± 2.8	1.13 ± 0.27	<0.02	0.19 ± 0.03	0.21 ± 0.02	3230 ± 130	-0.25 ± 0.25	(3)
LHS 6343c	12.713	62.9 ± 2.3	0.83 ± 0.02	0.056 ± 0.032	0.37 ± 0.01	0.38 ± 0.01	...	$+0.02 \pm 0.19$	4
LP 261-75b	1.882	68.1 ± 2.1	0.90 ± 0.02	<0.007	0.30 ± 0.02	0.31 ± 0.01	3100 ± 50	...	(5)
WASP-30b	4.157	61.0 ± 0.9	0.89 ± 0.02	0 (adopted)	1.17 ± 0.03	1.30 ± 0.02	6201 ± 97	-0.08 ± 0.10	(6)
WASP-128b	2.209	37.2 ± 0.9	0.94 ± 0.02	<0.007	1.16 ± 0.04	1.15 ± 0.02	5950 ± 50	$+0.01 \pm 0.12$	(7)
CoRoT-3b	4.257	21.7 ± 1.0	1.01 ± 0.07	0 (adopted)	1.37 ± 0.09	1.56 ± 0.09	6740 ± 140	-0.02 ± 0.06	(8)
CoRoT-15b	3.060	63.3 ± 4.1	1.12 ± 0.30	0 (adopted)	1.32 ± 0.12	1.46 ± 0.31	6350 ± 200	$+0.10 \pm 0.20$	(9)
CoRoT-33b	5.819	59.0 ± 1.8	1.10 ± 0.53	0.070 ± 0.002	0.86 ± 0.04	0.94 ± 0.14	5225 ± 80	$+0.44 \pm 0.10$	(10)
Kepler-39b	21.087	20.1 ± 1.3	1.24 ± 0.10	0.112 ± 0.057	1.29 ± 0.07	1.40 ± 0.10	6350 ± 100	$+0.10 \pm 0.14$	(11)
KOI-189b	30.360	78.0 ± 3.4	1.00 ± 0.02	0.275 ± 0.004	0.76 ± 0.05	0.73 ± 0.02	4952 ± 40	-0.07 ± 0.12	(12)
KOI-205b	11.720	39.9 ± 1.0	0.81 ± 0.02	<0.031	0.92 ± 0.03	0.84 ± 0.02	5237 ± 60	$+0.14 \pm 0.12$	(13)
KOI-415b	166.788	62.1 ± 2.7	0.79 ± 0.12	0.689 ± 0.001	0.94 ± 0.06	1.15 ± 0.15	5810 ± 80	-0.24 ± 0.11	(14)
EPIC 201702477b	40.737	66.9 ± 1.7	0.76 ± 0.07	0.228 ± 0.003	0.87 ± 0.03	0.90 ± 0.06	5517 ± 70	-0.16 ± 0.05	(15)
EPIC 212036875b	5.170	52.3 ± 1.9	0.87 ± 0.02	0.132 ± 0.004	1.29 ± 0.07	1.50 ± 0.03	6238 ± 60	$+0.01 \pm 0.10$	(18), (21)
AD 3116b	1.983	54.2 ± 4.3	1.02 ± 0.28	0.146 ± 0.024	0.28 ± 0.02	0.29 ± 0.08	3200 ± 200	$+0.16 \pm 0.10$	(17)
CWW 89Ab	5.293	39.2 ± 1.1	0.94 ± 0.02	0.189 ± 0.002	1.10 ± 0.05	1.03 ± 0.02	5755 ± 49	$+0.20 \pm 0.09$	(16), (18)
RIK 72b	97.760	59.2 ± 6.8	3.10 ± 0.31	0.146 ± 0.012	0.44 ± 0.04	0.96 ± 0.10	3349 ± 142	...	(19)
NGTS-7Ab	0.676	$75.5^{+3.0}_{-13.7}$	$1.38^{+0.13}_{-0.14}$	0 (adopted)	0.48 ± 0.13	0.61 ± 0.06	3359 ± 106	...	(20)
2M0535-05a	9.779	56.7 ± 4.8	6.50 ± 0.33	0.323 ± 0.006	(22)
2M0535-05b	9.779	35.6 ± 2.8	5.00 ± 0.25	0.323 ± 0.006	(22)

References. (1) Zhou et al. (2019), (2) Siverd et al. (2012), (3) Irwin et al. (2010), (4) Johnson et al. (2011), (5) Irwin et al. (2018), (6) Anderson et al. (2011), (7) Hodžić et al. (2018), (8) Deleuil et al. (2008), (9) Bouchy et al. (2011b), (10) Csizmadia et al. (2015), (11) Bonomo et al. (2015), (12) Díaz et al. (2014), (13) Díaz et al. (2013), (14) Moutou et al. (2013), (15) Bayliss et al. (2017), (16) Nowak et al. (2017), (17) Gillen et al. (2017), (18) Carmichael et al. (2019), (19) David et al. (2019), (20) Jackman et al. (2019), (21) Persson et al. (2019), (22) Stassun et al. (2006).

Goldreich & Soter (1966), from whom Jackson et al. (2008) obtained their expressions, did. Rewriting this expression to use the terminology of this work, the synchronization timescale is

$$\frac{1}{\tau_\Omega} = \frac{9}{4} \frac{GR_*^3 M_{\text{BD}}^2}{\alpha_* M_* Q_* \Omega a^6}, \quad (3)$$

where Ω is the angular velocity of the star.

Tidal quality factors are difficult to measure. There are only three BDs with published constraints on Q , which indicate $\log Q_{\text{BD}} > 4.15$ – 4.5 (Heller et al. 2010; Beatty et al. 2018). Furthermore, there is disagreement in the literature about the values of Q_* , with plausible values ranging from 10^4 to 10^8 ; furthermore, even for a single system the value of Q_* may change over time as the tidal forcing changes due to the orbital evolution of the system as well as stellar evolution (e.g., Jackson et al. 2008; Penev et al. 2012). Nonetheless, in order to assess the effect of the uncertain value of Q_* on the evolution of TOI-503, in Figure 13 we show the tidal damping timescales as a function of the tidal quality factors. As is apparent from the figure, the tidal timescales are shorter for the lower half of plausible values of Q_* and longer for the upper half.

We provide preferring values $Q_* = 10^8$ and $Q_{\text{BD}} = 10^5$ following Persson et al. (2019). These values have been chosen using the observational quantification of the dissipation of the stellar equilibrium tide by Collier Cameron & Jardine (2018) in hot-Jupiter systems and of the dissipation of tides in Jupiter by Lainey et al. (2009), respectively. Although EPIC 212036875 (Persson et al. 2019) is less massive than TOI-503, Collier Cameron & Jardine (2018) did not find any significant T_{eff} dependence of Q_* for the stellar equilibrium tide, justifying this assumption. For the orbital period larger than half of the

rotation period of the star, tidal inertial waves (i.e., one of the components of the dynamical tide; e.g., Ogilvie & Lin 2007) can be excited in convective regions (Bolmont & Mathis 2016). However, for a massive star such as TOI-503, the convective envelope should be very thin leading to a negligible dissipation of tidal inertial waves (Mathis 2015; Gallet et al. 2017), while this dissipation can also be neglected in the convective core because this is a full sphere (e.g., Ogilvie & Lin 2004; Wu 2005). At the same time, the presence of this core may prevent an efficient dissipation of tidal gravity waves propagating in the radiative layers of TOI-503 (Barker & Ogilvie 2010; Guillot et al. 2014). Therefore, the estimate we provide here using the equilibrium tide values should be reasonable. We also note that an alternative tidal model relying on dynamical tides within the radiative envelope of hot stars was presented by Zahn (1977); using this model, which may be more appropriate for a hot star like TOI-503, predicts tidal damping timescales more than an order of magnitude larger than the Jackson et al. (2008) model for the largest plausible values of Q_* . However, given this uncertainty in the appropriate tidal model and value of Q_* , we cannot draw any firm conclusions on the tidal evolution of the system.

4.3. TOI-503 in Context among Am-star Binaries

Am stars are commonly found in binary systems (e.g., Carquillat & Prieur 2007) and rotate more slowly than is typical for field A stars (e.g., Abt & Morrell 1995). The Am nature of these stars is thought to be due to their slow rotation, and it has been hypothesized that there may be a link between the binarity and slow rotation, but the exact mechanisms involved are still not well known (e.g., Böhm-Vitense 2006). It has also been

Table 6
Additional Information on Published Transiting Brown Dwarfs

Name	α_{J2000}	δ_{J2000}	V (magnitude)	Reference
TOI-503	08 17 16.89	12 36 04.76	9.40	this work
LP 261-75	09 51 04.58	+35 58 09.47	15.43	Irwin et al. (2018)
NLTT 41135	15 46 04.30	+04 41 30.06	18.00	Irwin et al. (2010)
LHS 6343	19 10 14.28	+46 57 24.11	13.39	Johnson et al. (2011)
KELT-1	00 01 26.92	+39 23 01.70	10.70	Sivervd et al. (2012)
HATS-70	07 16 25.08	−31 14 39.86	12.57	Zhou et al. (2019)
WASP-30	23 53 38.03	−10 07 05.10	12.00	Anderson et al. (2011)
WASP-128	11 31 26.10	−41 41 22.30	12.50	Hodžić et al. (2018)
CoRoT-3	19 28 13.26	+00 07 18.70	13.29	Deleuil et al. (2008)
CoRoT-15	06 28 27.82	+06 11 10.47	16.00	Bouchy et al. (2011b)
CoRoT-33	18 38 33.91	+05 37 28.97	14.70	Csizmadia et al. (2015)
Kepler-39	19 47 50.46	+46 02 03.49	14.47	Bouchy et al. (2011a)
KOI-189	18 59 31.19	+49 16 01.17	14.74	Díaz et al. (2014)
KOI-205	19 41 59.20	+42 32 16.41	14.85	Díaz et al. (2013)
KOI-415	19 33 13.45	+41 36 22.93	14.34	Moutou et al. (2013)
EPIC 201702477	11 40 57.79	+03 40 53.70	14.57	Bayliss et al. (2017)
EPIC 212036875	08 58 45.67	+20 52 08.73	10.95	Persson et al. (2019)
CWW 89A	19 17 34.04	−16 52 17.80	12.54	Nowak et al. (2017)
AD 3116	08 42 39.43	+19 24 51.90	18.73	Gillen et al. (2017)
NGTS-7A	23 30 05.20	−38 58 11.71	15.50	Jackman et al. (2019)
RIK 72	16 03 39.22	−18 51 29.72	16.01	David et al. (2019)
2M0535-05 ^a	05 35 21.85	−05 46 08.56	18.94G ^b	Stassun et al. (2006)

Notes.

^a The 2M0535-05 system is a brown-dwarf binary.

^b G-band magnitude from the *Gaia* mission.

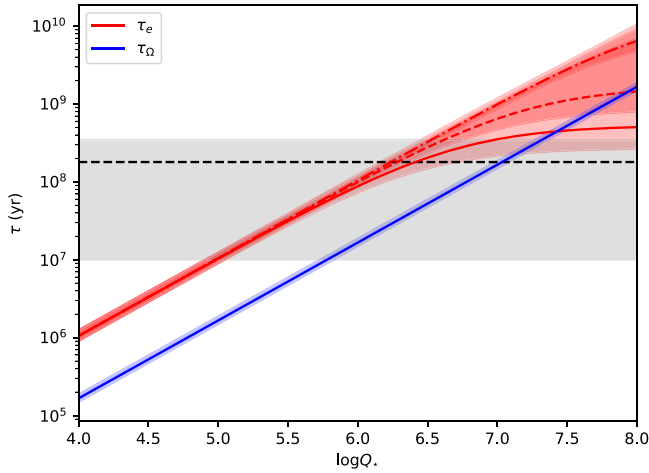


Figure 13. Values of the tidal circularization timescale τ_e (red line; Equation (2)) and tidal synchronization timescale τ_Ω (blue line; Equation (3)) as a function of stellar tidal quality factor Q_* . The solid, dashed, and dotted-dashed red lines correspond to values of the companion’s quality factor $\log Q_{BD} = 4.5, 5, 6$, respectively; these lines flatten at large Q_* as the dissipation in the brown dwarf begins to dominate the system, while we only show these lines for τ_e , as τ_Ω does not depend on Q_{BD} . The colored bands surrounding each line show the uncertainty on the timescale incorporating our measured uncertainties on the system parameters, but assuming Q_* , Q_{BD} fixed at the quoted values. The horizontal dashed line and gray region show the nominal system age and uncertainty therein, respectively.

noted that not all slowly rotating A stars are Am stars (Abt 2009). While many short-period Am binary systems could have experienced tidal synchronization, a significant number of Am binaries are too widely separated to experience significant tidal effects within their main-sequence lifetimes (Carquillat & Prieur 2007). Due to the systematic uncertainty on the tidal timescales for TOI-503 (Section 4.2), we cannot make any firm

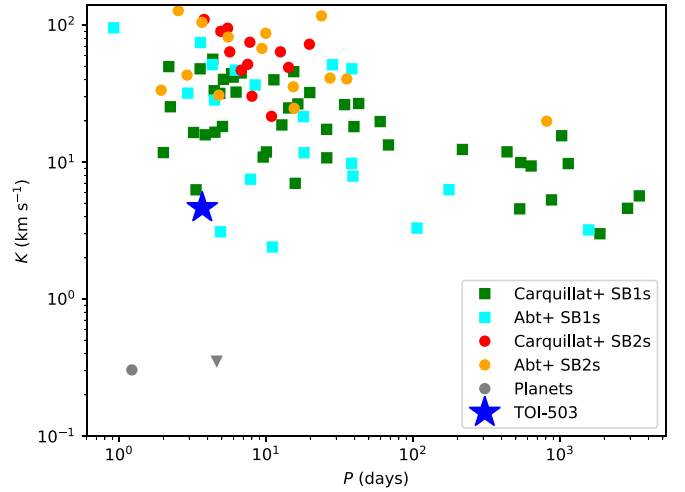


Figure 14. TOI-503 in context among the population of Am-star binaries from Abt & Levy (1985), Carquillat & Prieur (2007), and Smalley et al. (2014), as well as the planets WASP-33b and KELT-19Ab (the latter marked with a triangle, as there is only an upper mass limit available; Sivervd et al. 2018). The circles show SB2s where we have the RV semi-amplitude K for both components, while the squares show SB1s where we only have K for one component. TOI-503’s RV semi-amplitude is among the smallest of any known Am-star binary.

conclusions as to how any tidal braking experienced by the TOI-503 primary contributed to its nature as an Am star.

Although it lies at the lower end of the envelope in mass ratio, the TOI-503 system does not otherwise stand out significantly from the known population of Am binaries. In Figure 14 we show TOI-503 in context in the RV semi-amplitude-period plane for known Am-star binaries. TOI-503 has among the lowest K value of any known such system, but not the lowest. Boffin (2010) showed that the mass ratio

distribution of Am-star binaries is uniform, and in this context, the existence of TOI-503b at a very small mass ratio is not surprising. Future surveys more sensitive to very small mass ratio Am binaries will be necessary to determine whether the mass ratio distribution eventually tails off.

Apart from TOI-503, other Am stars known to host a low-mass companion ($M_b < 80M_J$) are WASP-33 (Collier Cameron et al. 2010b) and KELT-19A (Siverd et al. 2018), but the mass ratio q for both the systems is even smaller than the TOI-503 system.

4.4. How Did TOI-503b Form?

The age of TOI-503 is approximately 180 Myr. In Section 4.2, we have shown that given our consideration of the Jackson et al. (2008) and Zahn (1977) prescription of the tidal evolution of the system, we cannot say with certainty whether or not TOI-503 circularized the BD's orbit. Our interpretation of this is that TOI-503b may have formed at a larger orbital distance from its host star or also at a slightly larger eccentricity or more simply formed in situ in a nearly circular orbit.

Now the question becomes which formation mechanism (core accretion or fragmentation) is more plausible. To address this point, we can look at some of the nearest neighbors, in terms of mass, to TOI-503b: AD 3116b ($M_b = 54M_J$), EPIC 212036875b ($M_b = 52M_J$), and CWW 89Ab ($M_b = 39M_J$). As shown in two independent studies (Carmichael et al. 2019; Persson et al. 2019), EPIC 212036875b is an eccentric ($e = 0.132$), short-period ($P = 5.16$ days) BD that orbits an F-type star. The Persson et al. (2019) study found EPIC 212036875b to likely have formed farther from its host star via gravitational disk instabilities and then quickly migrate to its current, close-in eccentric orbit. This is argued because core accretion is not effective to grow a $50M_J$ object (Kratter & Lodato 2016), where fragmentation in the disk certainly could be, and this may be the case for TOI-503b.

For AD 3116b, the circularization timescale is challenging to interpret, as Gillen et al. (2017) caution, given the mass ratio of this system ($q \approx 0.18$), the very short (< 2 days) period, and the nature of the host M dwarf star. Though AD 3116b is young at a measured age of 600 Myr, given the nature of its orbit and host star, it is more difficult to infer a formation scenario. The narrative for CWW 89Ab is different still from these other examples, as Beatty et al. (2018) argue that it formed via core accretion in part of a triple system that includes a wide secondary star, CWW 89B. From these few examples, we see that a difference in mass of $39M_J$ (CWW 89Ab) versus $52M_J$ (EPIC 212036875b) may have origins in different formation scenarios. This highlights how the mass of a short-period BD may not as strongly dictate a formation scenario as any single discovery might imply and that there are plausible non-in-situ formation pathways that come from both core accretion or disk fragmentation.

On the other hand, the in situ formation scenario points to a possible way that Am stars can form. To our knowledge, this is the first time a BD has been detected orbiting an Am star in such a short period. Detailed studies of Am stars report a binary fraction around 60%–70% (Abt & Levy 1985; Carquillat & Prieur 2007). In some such systems, the stellar companions are too distant for the tidal braking to be effective (e.g., Siverd et al. 2018). It possibly suggests that other processes may need to be invoked to explain their small rotational velocities. However, this may also be linked to the fact that it is relatively

difficult to detect such a low-mass companion as a BD around an Am star, and our discovery of one such BD around an Am star in the BD desert may reflect this. However, further similar discoveries are needed to confirm if this is the correct explanation. The BD orbiting an Am star is a bridge connecting two areas that are not fully understood: the formation mechanisms and ultimate classification of BDs, and the creation, evolution, and behavior of Am stars. Such an overlap enables us to look at these areas from an entirely new perspective.






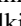



5. Summary

We have presented the analysis of the first BD known to transit an Am star, TOI-503b. This is the newest member of the BD desert, and it orbits its host star in a circular, short-period ($P = 3.67718 \pm 0.0001$ days) orbit. We measure the host star to have a mass of $M_* = 1.80 \pm 0.06 M_\odot$, a radius of $R_* = 1.70 \pm 0.05 R_\odot$, an effective temperature of $T_{\text{eff}} = 7650 \pm 160$ K, and metallicity of 0.6 ± 0.1 dex. The transit geometry of the system is grazing as revealed by the *TESS* light curve. The BD has a radius of $R_b = 1.34^{+0.26}_{-0.15} R_J$ and mass of $M_b = 53.7 \pm 1.2 M_J$, which places it in the driest part of the BD desert. The age of the system is estimated to be ~ 180 Myr using MIST and YY isochrones. Given the difficulty in measuring the tidal interactions between BDs and their host stars, we cannot make any firm conclusions whether this BD formed in situ or has had its orbit circularized by its host star. Instead, we offer an examination of plausible values for the tidal quality factor for the star and BD, and also provide the preferring value.

J.Š. and P.K. would like to acknowledge the support from GACR international grant 17-01752J. J.Š. would like to acknowledge the support from source 116-09/260441, Institute of Theoretical Physics, Charles University in Prague, Czech Republic. J.K., S.G., M.P., S.C., A.P.H., H.R., M.E., and K.W.F. L. acknowledge support by Deutsche Forschungsgemeinschaft (DFG) grants PA525/18-1, PA525/19-1, PA525/20-1, HA 3279/12-1, and RA 714/14-1 within the DFG Schwerpunkt SPP 1992, Exploring the Diversity of Extrasolar Planets. S.C. acknowledges the Hungarian Scientific Research Fund (OTKA) Grant KH-130372. This work is partly supported by JSPS KAKENHI grant Nos. JP18H01265 and JP18H05439, and JST PRESTO grant No. JPMJPR1775. S.M. acknowledges support by the Spanish Ministry through the Ramon y Cajal fellowship number RYC-2015-17697. R.A.G. acknowledges the support from the PLATO/CNES grant. M.S. acknowledges the Postdoc@MUNI project CZ.02.2.69/0.0/0.0/16-027/0008360. S. M. acknowledges support from the ERC SPIRE 647383 grant. M.F., C.M.P., and I.G. gratefully acknowledge the support of the Swedish National Space Agency (DNR 163/16 and 174/18). K. G.S. acknowledges partial support from NASA grant 17-XRP17 2-0024. This paper includes data collected by the *Kepler* mission. Funding for the *Kepler* mission is provided by the NASA Science Mission directorate. Some of the data presented in this paper were obtained from the Mikulski Archive for Space Telescopes (MAST). STScI is operated by the Association of Universities for Research in Astronomy, Inc., under NASA contract NAS5-26555. Based on observations made with the Nordic Optical Telescope, operated by the Nordic Optical Telescope Scientific Association at the Observatorio del Roque de los Muchachos, La Palma, Spain, of the Instituto de Astrofísica de Canarias. Also based in part on observations

collected at the European Organisation for Astronomical Research in the Southern Hemisphere under ESO program P103.C-0449. T.W.C. would like to acknowledge the effort of the observers who acquired the ground-based photometry at FLWO, LCO, CHAT, and FLI as part of the *TESS* Follow-up Program. Thanks to Alex J. Mustill and Scott Gaudi for useful discussions. The PARAS spectrograph is fully funded and being supported by Physical Research Laboratory (PRL), which is part of Department of Space, Government of India. R.S. and A.C. would like to thank Director P.R.L. for his support and acknowledges the help from Vishal Shah and the Mount Abu Observatory staff at the time of observations. A.C. is grateful to Suvrath Mahadevan from Pennsylvania State University and Arpita Roy from Caltech, for their tremendous efforts in the development of the PARAS data pipeline.

ORCID iDs

Ján Šubjak  <https://orcid.org/0000-0002-5313-9722>
 Rishikesh Sharma  <https://orcid.org/0000-0001-8983-5300>
 Theron W. Carmichael  <https://orcid.org/0000-0001-6416-1274>
 Marshall C. Johnson  <https://orcid.org/0000-0002-5099-8185>
 Henri M. J. Boffin  <https://orcid.org/0000-0002-9486-4840>
 Rafael Brahm  <https://orcid.org/0000-0002-9158-7315>
 Priyanka Chaturvedi  <https://orcid.org/0000-0002-1887-1192>
 Abhijit Chakraborty  <https://orcid.org/0000-0002-3815-8407>
 Karen A. Collins  <https://orcid.org/0000-0001-6588-9574>
 Malcolm Fridlund  <https://orcid.org/0000-0003-2180-9936>
 Tianjun Gan  <https://orcid.org/0000-0002-4503-9705>
 Davide Gandolfi  <https://orcid.org/0000-0001-8627-9628>
 David W. Latham  <https://orcid.org/0000-0001-9911-7388>
 Savita Mathur  <https://orcid.org/0000-0002-0129-0316>
 Joshua E. Schlieder  <https://orcid.org/0000-0001-5347-7062>
 Thomas Barclay  <https://orcid.org/0000-0001-7139-2724>
 Courtney D. Dressing  <https://orcid.org/0000-0001-8189-0233>
 Andrew W. Howard  <https://orcid.org/0000-0001-8638-0320>
 George Zhou  <https://orcid.org/0000-0002-4891-3517>
 Samuel N. Quinn  <https://orcid.org/0000-0002-8964-8377>
 Michael L. Calkins  <https://orcid.org/0000-0002-2830-5661>
 Keivan G. Stassun  <https://orcid.org/0000-0002-3481-9052>
 Marek Skarka  <https://orcid.org/0000-0002-7602-0046>
 Jiří Žák  <https://orcid.org/0000-0001-9416-9007>
 Juan Cabrera  <https://orcid.org/0000-0001-6653-5487>
 William D. Cochran  <https://orcid.org/0000-0001-9662-3496>
 Fei Dai  <https://orcid.org/0000-0002-8958-0683>
 Hans J. Deeg  <https://orcid.org/0000-0003-0047-4241>
 Michael Endl  <https://orcid.org/0000-0002-7714-6310>
 Akihiko Fukui  <https://orcid.org/0000-0002-4909-5763>
 Sascha Grziwa  <https://orcid.org/0000-0003-3370-4058>
 Teruyuki Hirano  <https://orcid.org/0000-0003-3618-7535>
 John H. Livingston  <https://orcid.org/0000-0002-4881-3620>
 Mikkel N. Lund  <https://orcid.org/0000-0001-9214-5642>
 Pilar Montanes Rodríguez  <https://orcid.org/0000-0002-6855-9682>
 Norio Narita  <https://orcid.org/0000-0001-8511-2981>
 Prajwal Niraula  <https://orcid.org/0000-0002-8052-3893>

Grzegorz Nowak  <https://orcid.org/0000-0002-7031-7754>
 Seth Redfield  <https://orcid.org/0000-0003-3786-3486>
 Ignasi Ribas  <https://orcid.org/0000-0002-6689-0312>
 Alexis M. S. Smith  <https://orcid.org/0000-0002-2386-4341>
 Vincent Van Eylen  <https://orcid.org/0000-0001-5542-8870>
 Petr Kabáth  <https://orcid.org/0000-0002-1623-5352>

References

- Abt, H. A. 2009, *AJ*, **138**, 28
 Abt, H. A., & Levy, S. G. 1985, *ApJS*, **59**, 229
 Abt, H. A., & Morrell, N. I. 1995, *ApJS*, **99**, 135
 Abt, H. A., & Moyn, K. I. 1973, *ApJ*, **182**, 809
 Aigrain, S., Llama, J., Ceillier, T., et al. 2015, *MNRAS*, **450**, 3211
 Albrecht, S., Reffert, S., Snellen, I., Quirrenbach, A., & Mitchell, D. S. 2007, *A&A*, **474**, 565
 Alsubai, K., Tsvetanov, Z. I., Latham, D. W., et al. 2018, *AJ*, **155**, 52
 Amôres, E. B., & Lépine, J. R. D. 2005, *AJ*, **130**, 659
 Anderson, D. R., Collier Cameron, A., Hellier, C., et al. 2011, *ApJL*, **726**, L19
 Balona, L. A. 2011, *MNRAS*, **415**, 1691
 Balona, L. A. 2013, *MNRAS*, **431**, 2240
 Balona, L. A. 2017, *MNRAS*, **467**, 1830
 Balona, L. A., Catanzaro, G., Abedigamba, O. P., Ripepi, V., & Smalley, B. 2015, *MNRAS*, **448**, 1378
 Baraffe, I., Chabrier, G., Allard, F., & Hauschildt, P. H. 2002, *A&A*, **382**, 563
 Baraffe, I., Chabrier, G., Barman, T. S., Allard, F., & Hauschildt, P. H. 2003, *A&A*, **402**, 701
 Barker, A. J., & Ogilvie, G. I. 2010, *MNRAS*, **404**, 1849
 Barragán, O., Gandolfi, D., & Antoniciello, G. 2019, *MNRAS*, **482**, 1017
 Bayliss, D., Hojatpanah, S., Santerne, A., et al. 2017, *AJ*, **153**, 15
 Beatty, T. G., Morley, C. V., Curtis, J. L., et al. 2018, *AJ*, **156**, 168
 Blanco-Cuaresma, S. 2019, *MNRAS*, **486**, 2075
 Blanco-Cuaresma, S., Soubiran, C., Heiter, U., & Jofré, P. 2014, *A&A*, **569**, A111
 Boffin, H. M. J. 2010, *A&A*, **524**, A14
 Böhm, T., Holschneider, M., Lignières, F., et al. 2015, *A&A*, **577**, A64
 Böhm-Vitense, E. 2006, *PASP*, **118**, 419
 Bolmont, E., & Mathis, S. 2016, *CeMDA*, **126**, 275
 Bonomo, A. S., Sozzetti, A., Santerne, A., et al. 2015, *A&A*, **575**, A85
 Borucki, W. J., Koch, D., Basri, G., et al. 2010, *Sci*, **327**, 977
 Bouchy, F., Bonomo, A. S., Santerne, A., et al. 2011a, *A&A*, **533**, A83
 Bouchy, F., Deleuil, M., Guillot, T., et al. 2011b, *A&A*, **525**, A68
 Bressan, A., Marigo, P., Girardi, L., et al. 2012, *MNRAS*, **427**, 127
 Buchhave, L. A., Bakos, G. Á., Hartman, J. D., et al. 2010, *ApJ*, **720**, 1118
 Buchhave, L. A., Latham, D. W., Johansen, A., et al. 2012, *Natur*, **486**, 375
 Carmichael, T., Latham, D., & Vanderburg, A. 2019, *AJ*, **158**, 38
 Carquillat, J.-M., & Prieur, J.-L. 2007, *MNRAS*, **380**, 1064
 Cayrel, R., van't Veer-Menneret, C., Allard, N. F., & Stehlé, C. 2011, *A&A*, **531**, A83
 Ceillier, T., Tayar, J., Mathur, S., et al. 2017, *A&A*, **605**, A111
 Ceillier, T., van Saders, J., García, R. A., et al. 2016, *MNRAS*, **456**, 119
 Chakraborty, A., Mahadevan, S., Roy, A., et al. 2014, *PASP*, **126**, 133
 Chaturvedi, P., Chakraborty, A., Anandarao, B. G., Roy, A., & Mahadevan, S. 2016, *MNRAS*, **462**, 554
 Chaturvedi, P., Sharma, R., Chakraborty, A., Anandarao, B. G., & Prasad, N. J. S. S. V. 2018, *AJ*, **156**, 27
 Choi, J., Dotter, A., Conroy, C., et al. 2016, *ApJ*, **823**, 102
 Claret, A. 2017, *A&A*, **600**, A30
 Claret, A., & Gimenez, A. 1989, *A&AS*, **81**, 37
 Coleman, G. A. L., Papaloizou, J. C. B., & Nelson, R. P. 2017, *MNRAS*, **470**, 3206
 Collier Cameron, A., Bruce, V. A., Miller, G. R. M., Triaud, A. H. M. J., & Queloz, D. 2010a, *MNRAS*, **403**, 151
 Collier Cameron, A., Guenther, E., Smalley, B., et al. 2010b, *MNRAS*, **407**, 507
 Collier Cameron, A., Horne, K., Penny, A., & Leigh, C. 2002, *MNRAS*, **330**, 187
 Collier Cameron, A., & Jardine, M. 2018, *MNRAS*, **476**, 2542
 Collins, K. A., Kielkopf, J. F., Stassun, K. G., & Hessman, F. V. 2017, *AJ*, **153**, 77
 Csizmadia, S. & CoRoT Team 2016, in *The CoRoT Legacy Book: The adventure of the ultra high precision photometry from space*, ed. CoRoT Team (Les Ulis: EDP Sciences), 143
 Csizmadia, S., Hatzes, A., Gandolfi, D., et al. 2015, *A&A*, **584**, A13

- Cutri, R. M., Skrutskie, M. F., van Dyk, S., et al. 2003, *yCat*, **2246**, 0
- Cutri, R. M., Wright, E. L., Conrow, T., et al. 2013, *yCat*, **2328**, 0
- da Silva, L., Girardi, L., Pasquini, L., et al. 2006, *A&A*, **458**, 609
- David, T. J., Hillenbrand, L. A., Gillen, E., et al. 2019, *ApJ*, **872**, 161
- Deleuil, M., Deeg, H. J., Alonso, R., et al. 2008, *A&A*, **491**, 889
- Díaz, R. F., Damiani, C., Deleuil, M., et al. 2013, *A&A*, **551**, L9
- Díaz, R. F., Montagnier, G., Leconte, J., et al. 2014, *A&A*, **572**, A109
- Dotter, A. 2016, *ApJS*, **222**, 8
- Eastman, J. D., Rodriguez, J. E., Agol, E., et al. 2019, arXiv:1907.09480
- Frandsen, S., & Lindberg, B. 1999, in *Proc. Astrophysics with the NOT*, ed. H. Karttunen & V. Pirola (Piikkio: Univ. Turku), 71
- Furlan, E., Ciardi, D. R., Everett, M. E., et al. 2017, *AJ*, **153**, 71
- Gallet, F., Bolmont, E., Mathis, S., Charbonnel, C., & Amard, L. 2017, *A&A*, **604**, A112
- Gandolfi, D., Fossati, L., Livingston, J. H., et al. 2019, *ApJL*, **876**, L24
- Gandolfi, D., Parviainen, H., Deeg, H. J., et al. 2015, *A&A*, **576**, A11
- García, R. A., Ceillier, T., Salabert, D., et al. 2014a, *A&A*, **572**, A34
- García, R. A., Mathur, S., Pires, S., et al. 2014b, *A&A*, **568**, A10
- Gibson, N. P., Aigrain, S., Roberts, S., et al. 2012, *MNRAS*, **419**, 2683
- Gillen, E., Hillenbrand, L. A., David, T. J., et al. 2017, *ApJ*, **849**, 11
- Goldreich, P., & Soter, S. 1966, *Icar*, **5**, 375
- Grether, D., & Lineweaver, C. H. 2006, *ApJ*, **640**, 1051
- Guillot, T., Lin, D. N. C., Morel, P., Havel, M., & Parmentier, V. 2014, in *Evolution of Exoplanets and Their Parent Stars*, EAS Publications Ser., Vol 65, ed. Y. Lebreton, D. Valls-Gabaud, & C. Charbonnel (Cambridge: Cambridge Univ. Press), 327
- Gustafsson, B., Edvardsson, B., Eriksson, K., et al. 2008, *A&A*, **486**, 951
- Hale, A. 1994, *AJ*, **107**, 306
- Hatzes, A. P. 1998, *A&A*, **330**, 541
- Hatzes, A. P., & Rauer, H. 2015, *ApJL*, **810**, L25
- Heiter, U., Lind, K., Asplund, M., et al. 2015, *PhysS*, **90**, 054010
- Heller, R., Jackson, B., Barnes, R., Greenberg, R., & Homeier, D. 2010, *A&A*, **514**, A22
- Hjorth, M., Justesen, A. B., Hirano, T., et al. 2019, *MNRAS*, **484**, 3522
- Hodžić, V., Triaid, A. H. M. J., Anderson, D. R., et al. 2018, *MNRAS*, **481**, 5091
- Høg, E., Fabricius, C., Makarov, V. V., et al. 2000, *A&A*, **357**, 367
- Hut, P. 1980, *A&A*, **92**, 167
- Irwin, J., Buchhave, L., Berta, Z. K., et al. 2010, *ApJ*, **718**, 1353
- Irwin, J. M., Charbonneau, D., Esquerdo, G. A., et al. 2018, *AJ*, **156**, 140
- Jackman, J. A. G., Wheatley, P. J., Bayliss, D., et al. 2019, *MNRAS*, **489**, 5146
- Jackson, B., Greenberg, R., & Barnes, R. 2008, *ApJ*, **678**, 1396
- Jenkins, J. M., Twicken, J. D., McCauliff, S., et al. 2016, *Proc. SPIE*, **9913**, 99133E
- Johnson, J. A., Apps, K., Gazak, J. Z., et al. 2011, *ApJ*, **730**, 79
- Johnson, M. C., Dai, F., Justesen, A. B., et al. 2018, *MNRAS*, **481**, 596
- Kabáth, P., Skarka, M., Sabotta, S., et al. 2020, *PASP*, **132**, 035002
- Kabáth, P., Skarka, M., Sabotta, S., & Guenther, E. 2019a, *CoSka*, **49**, 462
- Kabáth, P., Žák, J., Boffin, H. M. J., et al. 2019b, *PASP*, **131**, 085001
- Korth, J., Csizmadia, S., Gandolfi, D., et al. 2019, *MNRAS*, **482**, 1807
- Kratter, K., & Lodato, G. 2016, *ARA&A*, **54**, 271
- Kurucz, R. L. 1993, *SYNTHES Spectrum Synthesis Programs and Line Data*, Kurucz CD-ROM, Smithsonian Astrophysical Observatory
- Lainey, V., Arlot, J.-E., Karatekin, Ö., & van Hoolst, T. 2009, *Natur*, **459**, 957
- Lindgren, L., Hernández, J., Bombrun, A., et al. 2018, *A&A*, **616**, A2
- Livingston, J. H., Dai, F., Hirano, T., et al. 2019, *MNRAS*, **484**, 8
- Lucy, L. B., & Sweeney, M. A. 1971, *AJ*, **76**, 544
- Ma, B., & Ge, J. 2014, *MNRAS*, **439**, 2781
- Mann, A. W., Gaidos, E., Mace, G. N., et al. 2016, *ApJ*, **818**, 46
- Mathis, S. 2015, *A&A*, **580**, L3
- Mathur, S., García, R. A., Régulo, C., et al. 2010, *A&A*, **511**, A46
- McQuillan, A., Mazeh, T., & Aigrain, S. 2014, *ApJS*, **211**, 24
- Meschiari, S., Wolf, A. S., Rivera, E., et al. 2009, *PASP*, **121**, 1016
- Michaud, G., Tarasick, D., Charland, Y., & Pelletier, C. 1983, *ApJ*, **269**, 239
- Mordasini, C., Alibert, Y., Klahr, H., & Henning, T. 2012, *A&A*, **547**, A111
- Moutou, C., Bonomo, A. S., Bruno, G., et al. 2013, *A&A*, **558**, L6
- Ni, D. 2018, *A&A*, **613**, A32
- Nowak, G., Palle, E., Gandolfi, D., et al. 2017, *AJ*, **153**, 131
- Ogilvie, G. I., & Lin, D. N. C. 2004, *ApJ*, **610**, 477
- Ogilvie, G. I., & Lin, D. N. C. 2007, *ApJ*, **661**, 1180
- Palle, E., Nowak, G., Luque, R., et al. 2019, *A&A*, **623**, A41
- Paunzen, E. 2015, *A&A*, **580**, A23
- Paxton, B., Marchant, P., Schwab, J., et al. 2015, *ApJS*, **220**, 15
- Penev, K., Jackson, B., Spada, F., & Thom, N. 2012, *ApJ*, **751**, 96
- Persson, C. M., Csizmadia, S., Mustill, A. J., et al. 2019, *A&A*, **628**, A64
- Petit, P., Hébrard, E. M., Böhm, T., Folsom, C. P., & Lignières, F. 2017, *MNRAS*, **472**, L30
- Pires, S., Mathur, S., García, R. A., et al. 2015, *A&A*, **574**, A18
- Piskunov, N. E., & Valenti, J. A. 2002, *A&A*, **385**, 1095
- Ricker, G. R., Winn, J. N., Vanderspek, R., et al. 2015, *JATIS*, **1**, 014003
- Rouan, D., Baglin, A., Copet, E., et al. 1998, *EM&P*, **81**, 79
- Sabotta, S., Kabath, P., Korth, J., et al. 2019, *MNRAS*, **489**, 2069
- Sahlmann, J., Ségransan, D., Queloz, D., et al. 2011, *A&A*, **525**, A95
- Santos, A. R. G., García, R. A., Mathur, S., et al. 2019, *ApJS*, **244**, 21
- Saumon, D., & Marley, M. S. 2008, *ApJ*, **689**, 1327
- Schlegel, D. J., Finkbeiner, D. P., & Davis, M. 1998, *ApJ*, **500**, 525
- Siverd, R. J., Beatty, T. G., Pepper, J., et al. 2012, *ApJ*, **761**, 123
- Siverd, R. J., Collins, K. A., Zhou, G., et al. 2018, *AJ*, **155**, 35
- Skarka, M., Kabáth, P., Paunzen, E., et al. 2019, *MNRAS*, **487**, 4230
- Skrzypek, N., Warren, S. J., & Faherty, J. K. 2016, *A&A*, **589**, A49
- Smalley, B., Southworth, J., Pintado, O. I., et al. 2014, *A&A*, **564**, A69
- Smith, J. C., Stumpe, M. C., Van Cleve, J. E., et al. 2012, *PASP*, **124**, 1000
- Spada, F., Demarque, P., Kim, Y.-C., & Sills, A. 2013, *ApJ*, **776**, 87
- Spiegel, D. S., Burrows, A., & Milsom, J. A. 2011, *ApJ*, **727**, 57
- Stassun, K. G., Collins, K. A., & Gaudi, B. S. 2017, *AJ*, **153**, 136
- Stassun, K. G., Corsaro, E., Pepper, J. A., & Gaudi, B. S. 2018a, *AJ*, **155**, 22
- Stassun, K. G., Mathieu, R. D., & Valenti, J. A. 2006, *Natur*, **440**, 311
- Stassun, K. G., Oelkers, R. J., Pepper, J., et al. 2018b, *AJ*, **156**, 102
- Stassun, K. G., & Torres, G. 2016, *ApJL*, **831**, L6
- Stassun, K. G., & Torres, G. 2018, *ApJ*, **862**, 61
- Stumpe, M. C., Smith, J. C., Catanzarite, J. H., et al. 2014, *PASP*, **126**, 100
- Telting, J. H., Avila, G., Buchhave, L., et al. 2014, *AN*, **335**, 41
- Tody, D. 1993, in *ASP Conf. Ser. 52, Astronomical Data Analysis Software and Systems II*, ed. R. J. Hanisch, R. J. V. Brissenden, & J. Barnes (San Francisco, CA: ASP), 173
- Torrence, C., & Compo, G. P. 1998, *BAMS*, **79**, 61
- Torres, G., Andersen, J., & Giménez, A. 2010, *A&ARv*, **18**, 67
- Udry, S., Mayor, M., & Queloz, D. 1999, in *ASP Conf. Ser. 185, IAU Coll. 170: Precise Stellar Radial Velocities*, ed. J. B. Hearnshaw & C. D. Scarfe (San Francisco, CA: ASP), 367
- van Dokkum, P. G. 2001, *PASP*, **113**, 1420
- Whitworth, A. 2018, in *Handbook of Exoplanets*, ed. H. J. Deeg (Cham: Springer), 1
- Wizinowich, P., Acton, D. S., Shelton, C., et al. 2000, *PASP*, **112**, 315
- Wu, Y. 2005, *ApJ*, **635**, 674
- Zahn, J.-P. 1977, *A&A*, **57**, 383
- Zhou, G., Bakos, G. Á., Bayliss, D., et al. 2019, *AJ*, **157**, 31